Breaking of Internal Waves and Turbulent Dissipation in an Anticyclonic Mode Water Eddy

Bieito Fernández-Castro * † ‡, Dafydd Gwyn Evans, Eleanor Frajka-Williams

National Oceanography Centre, SO14 3ZH, Southampton, UK

Clément Vic

Laboratoire d'Océanographie Physique et Spatiale, UBO-CNRS-IFREMER-IRD, IUEM, 29280, Plouzané, France

Alberto C. Naveira-Garabato

Ocean and Earth Science, National Oceanography Centre, University of Southampton, SO14 3ZH, Southampton, UK

[*] *Corresponding author address:* Physics of Aquatic Systems Laboratory (APHYS), École Polytechnique Fédérale de Lausanne (EPFL), CH-1015, Lausanne, Switzerland

E-mail: bieito.fernandezcastro@epfl.ch

[†] Departamento de Oceanografía, Instituto de Investigacións Mariñas (IIM-CSIC), 36208, Vigo, Spain

[‡] Physics of Aquatic Systems Laboratory (APHYS), École Polytechnique Fédérale de Lausanne (EPFL), CH-1015, Lausanne, Switzerland

Early Online Release: This preliminary version has been accepted for publication in *Journal of the Physical Oceanography*, may be fully cited, and has been assigned DOI 10.1175/JPO-D-19-0168.1. The final typeset copyedited article will replace the EOR at the above DOI when it is published.

ABSTRACT

A four-month glider mission was analyzed to assess turbulent dissipation in an anticyclonic eddy at the western boundary of the subtropical North Atlantic. The eddy (radius ≈ 60 km) had a core of low potential vorticity between 100–450 m, with maximum radial velocities of 0.5 m s^{-1} and Rossby number ≈ -0.1. Turbulent dissipation was inferred from vertical water velocities derived from the glider flight model. Dissipation was suppressed in the eddy core ($\varepsilon \approx 5 \times 10^{-10}$ W kg^{-1}) and enhanced below it ($> 10^{-9}$ W kg^{-1}). Elevated dissipation was coincident with quasi-periodic structures in the vertical velocity and pressure perturbations, suggesting internal waves as the drivers of dissipation. A heuristic ray-tracing approximation was used to investigate the wave-eddy interactions leading to turbulent dissipation. Ray-tracing simulations were consistent with two types of wave-eddy interactions that may induce dissipation: the trapping of near-inertial wave energy by the eddy's relative vorticity, or the entry of an internal tide (generated at the nearby continental slope) to a critical layer in the eddy shear. The latter scenario suggests that the intense mesoscale field characterizing the western boundaries of ocean basins might act as a 'leaky wall' controlling the propagation of internal tides into the basins' interior.

Accepted for publication in *Journal of Physical Oceanography*. DOI 10.1175/JPO-D-19-0168.1.

1. Introduction

Ocean turbulence plays a fundamental role in the transport of heat, freshwater, dissolved gases and other tracers in the ocean. By driving irreversible diapycnal mixing, turbulent motions maintain deep-ocean stratification and supply the potential energy needed to close the meridional overturning circulation (Munk and Wunsch 1998). The bulk of the power required to produce this interior turbulent mixing is thought to be provided by the breaking of internal waves (Wunsch and Ferrari 2004). Globally, there is a remarkable geographical variability in the distribution of turbulent mixing, which is possibly associated with variability in internal wave dissipation (Waterhouse et al. 2014; Kunze 2017; Whalen et al. 2012). In turn, recent modelling studies have shown that the geographical distribution and variability of mixing can have a strong impact on the predicted ocean state and meridional overturning (Melet et al. 2013, 2016). The temporal variability and geographical distribution of internal wave dissipation are dependent on the spatio-temporal structure of sources and the complex, and often poorly understood, interactions experienced by the waves on their propagation path (MacKinnon et al. 2017; Vic et al. 2019).

Different generation mechanisms produce internal waves of a range of wavenumbers and frequencies. Tidal and near-inertial frequencies are the most energetic wavebands in the internal wave spectrum, and associated waves are thought to be the main contributors to mixing in the ocean interior (MacKinnon et al. 2017). Internal tides are internal waves of tidal frequency generated when barotropic tides flow over rough topography (Egbert and Ray 2000; Nycander 2005), while near-inertial waves are often excited when variable wind stress induces a resonant response in the mixed-layer at the local inertial frequency (f) that propagates into the stratified ocean (Alford et al. 2016). Depending on their wavenumber and frequency, propagating waves can experience a wide range of interactions with the background flow and stratification (Munk 1981; Olbers 1981), to-

Accepted for publication in *Journal of Physical Oceanography*. DOI 10.1175/JPO-D-19-0168.1.

pography (Müller and Xu 1992; Nash et al. 2004) or other waves (Müller et al. 1986; Henyey et al. 1986) that result in wave dissipation and turbulent mixing. At the generation site, internal waves can have a complex vertical structure, often described as a sum of vertical modes (Alford 2003; Alford et al. 2016). Small-scale, high-mode waves are more prone to instability than larger-scale, low-mode waves (Olbers 1976), which may propagate over long distances and drive dissipation far away from their source (Alford 2003; Zhao et al. 2009). Low-mode (typically < 4) internal tides have long horizontal wavelengths ($\mathcal{O}(10-100)$ km) and high group velocities ($\mathcal{O}(1)$ m s^{-1}) and, as a result, interact weakly with the background flow (Rainville and Pinkel 2006). Low-mode waves can travel thousands of kilometers before dissipating (Zhao et al. 2016; de Lavergne et al. 2019), possibly through interactions with rough or sloping topography (Legg and Adcroft 2003; Nash et al. 2004; Bühler and Holmes-Cerfon 2011; Kelly et al. 2013). Higher-mode internal tides tend to break close to their topographic source, enhancing local mixing (St. Laurent and Garrett 2002). Their decay is mainly attributed to wave-wave interactions, though this remains a poorly quantified dissipation pathway (de Lavergne et al. 2019; Vic et al. 2019).

Mesoscale eddies, swirling vortices of water a few 10s of km to $\sim$200 km across, depending on the latitude, are ubiquitous in the world's oceans. They are highly energetic, dominating the ocean's kinetic energy reservoir at sub-inertial frequencies (Ferrari and Wunsch 2009). Mesoscale eddies are generated mainly by baroclinic instabilities (Smith 2007), they can persist for several months, and tend to propagate westward due to the Earth's rotation and curvature (Chelton et al. 2007, 2011). As a consequence of this westward drift and of the presence of strongly baroclinic western boundary currents favorable to baroclinic instability, eddies are abundant in the western sides of ocean basins (Chelton et al. 2007, 2011). Mesoscale eddies modify the background stratification and currents, affecting the propagation and dissipation of internal waves through linear and non-linear interactions (Kunze et al. 1995; Bühler and McIntyre 2005; Rainville and Pinkel

Accepted for publication in *Journal of Physical Oceanography*. DOI 10.1175/JPO-D-19-0168.1.

2006; Polzin 2010; Dunphy and Lamb 2014; Huang et al. 2018), as documented by several studies founded on the analysis of microstructure measurements or tracer release experiments (Lueck and Osborn 1986; Ledwell et al. 2008; Sheen et al. 2015; Fer et al. 2018).

Near-inertial waves have low frequency, slow horizontal and vertical group velocities, and spatial scales that overlap and favor interaction with mesoscale eddies (Weller 1982; Alford et al. 2016). The relative vorticity within the eddies ($\zeta = \partial_y u - \partial_x v$, where u is zonal velocity and v meridional velocity) can shift the resonant frequency of near-inertial motions to $f_{eff} \approx f + \zeta/2$ (Kunze 1985), where f is the inertial frequency, such that the near-inertial energy can be trapped and focused in the region of negative vorticity (Lonergan and White 1997; Joyce et al. 2013). This effect has been shown to be relevant for the temporal and large-scale geographical distribution of internal wave driven-turbulent dissipation (Whalen et al. 2012, 2018; Zhang et al. 2018). In contrast, generally weaker interactions (refraction and scattering to higher modes) occur between low-mode internal tides and the mesoscale field. This interactions manifest as a loss of coherence in the waves' long-range propagation (Rainville and Pinkel 2006; Nash et al. 2012; Kerry et al. 2014). Further, owing to their smaller size and group velocities, high-mode internal tides are more susceptible to undergo interactions with eddies than their low-mode counterparts. Such interactions can result in dissipation. However, this dissipation pathway is scarcely documented at present, and stands out as a key unknown contribution to the geography of internal tide dissipation (de Lavergne et al. 2019; Vic et al. 2019).

In this paper, we present results from a four-month glider mission that sampled an anticyclonic mesoscale eddy located at the western boundary of the North Atlantic subtropical gyre, at 26°N west of the Great Abaco Island (Bahamas). The observed variability of turbulent kinetic energy (TKE) dissipation rates within the eddy, inferred from glider-derived vertical seawater velocities using a large-eddy approximation (Beaird et al. 2015; Evans et al. 2018), was found to be consis-

Accepted for publication in *Journal of Physical Oceanography*. DOI 10.1175/JPO-D-19-0168.1.

tent with the breaking of internal waves due to eddy-wave interactions. After describing the data collection procedures and methodologies (section 2), we present the general hydrographic conditions and the characteristics of the anticyclonic eddy, as well as the distribution of TKE dissipation, in section 3. An interpretation of the observed dissipation in terms of eddy-wave interactions is provided, and the origin and characteristics of the waves are assessed using a heuristic ray-tracing approximation. Finally, the relevance and implications of the results are discussed in section 4.

2. Data collection and methods

a. Seaglider deployment and hydrographic data

Hydrographic data were collected using a Seaglider (sg534). Seagliders are autonomous underwater vehicles that control their buoyancy by pumping oil in and out of an external bladder, thus varying their density by adjusting their volume (Eriksen et al. 2001). The Seaglider was equipped with pressure, temperature and conductivity sensors (SeaBird CT sail), an Aanderaa optode designed to measure dissolved oxygen and a WETLabs Eco Puck optical sensor. The sg534 was deployed on the 7th of November 2017 and recovered on the 10th of March 2018 aboard *R/V F. G. Walton Smith* during two research cruises (WS17305, WS18066) as part of the MerMEED (Mechanisms responsible for Mesoscale Eddy Energy Dissipation) project. Additional gliders were deployed, but their missions were cut short. During its mission, the Seaglider profiled the water column with a vertical speed of 0.07-0.15 m s^{-1} between the surface and 1000 m in a saw-tooth fashion, performing a total of 1298 profiles (649 dives and climbs) in the vicinity of the continental slope between 26-27°N and 75-77°W (Figure 1a). The mean horizontal resolution was 2.3 km, ranging from 0.2 km (5%-percentile) to 7 km (95%-percentile), depending on the

Accepted for publication in *Journal of Physical Oceanography*. DOI 10.1175/JPO-D-19-0168.1.

background flow and the glider piloting. With a sampling rate of 0.1 Hz, the vertical resolution was of $\mathscr{O}(1\ \mathrm{m})$.

Initially, the quality of the temperature (T) and salinity (S) data was assessed by visual inspection of the potential temperature (θ) and salinity time series, and θ-S diagram (Figure 1b). This diagram was compared with data obtained from 155 θ-S profiles collected during the deployment and recovery cruises (6–9 November 2017 and 11–14 March 2018) with a pumped SeaBird conductivity-temperature-depth (CTD) sensor mounted onto two VMP-2000 tethered vertical microstructure profilers (Rockland Scientific International, RSI). This analysis revealed a relatively large spread in the glider salinity data associated with a salinity jump of -0.0764 ± 0.0018 on 26 February. This was removed by applying a fixed offset. After this correction, a small number (104 out of 239031 data points) of remaining anomalous salinity peaks apparent in the θ-S time series and θ-S diagram were also removed. The oxygen sensor was not calibrated during the cruises and hence, it could only be used for a qualitative interpretation of the observations. In order to obtain meaningful values of oxygen concentration, these were adjusted by adding a constant such that the cruise-mean oxygen concentration in the upper 10 m matched concentration at saturation. As the interval between glider CTD measurements was uneven in depth due to variable glider speeds and sample rates, the data were bin-averaged into 5-dbar bins.

The interpretation of the glider observations was aided by maps of sea level anomaly (SLA) and surface geostrophic velocity, obtained from the gridded ($0.25^\circ \times 0.25^\circ$) daily global near-real time fields produced by the Sea Level Thematic Assembly Centre of the Copernicus Marine Environment Monitoring Service (CMEMS) available at `https://marine.copernicus.eu`. Meteorological data (wind stress at 10 m and air-sea heat and freshwater fluxes) was taken from the 0.75° 3-hourly ERA-Interim global atmospheric reanalysis product (Dee et al. 2011). The grid cell lo-

Accepted for publication in *Journal of Physical Oceanography*. DOI 10.1175/JPO-D-19-0168.1.

cated closest to the center of the region sampled by the glider (26.25°N−75.75°W) was used in this analysis.

b. Turbulent kinetic energy dissipation inferred from the Seaglider

The spatial scales at which molecular viscosity dissipates TKE are on the order of several millimeters, and could not be directly resolved by our glider sampling approach. Instead, TKE dissipation rates (ε) were estimated using the large-eddy method (LEM) (Peters et al. 1995; Moum 1996; Gargett 1999) based on the quantification of TKE in the energy-containing scales of turbulence, $\mathscr{O}(0.1-10)$ m, which are at least an order of magnitude larger than the viscous scales. In this approximation, ε is proportional to the ratio between the TKE ($\sim u^2$, where u represents the turbulent velocity fluctuations) in the energy-containing scales and an overturn time-scale ($\tau \sim l/u$, where l is the characteristic length of turbulent overturns), i.e.

$$\varepsilon \sim \frac{u^2}{\tau} \sim \frac{u^3}{l} \,. \tag{1}$$

This approximation is based on the notion that TKE in the energy-containing eddies cascades down towards smaller scales, where viscous dissipation occurs (Kolmogorov 1941). Additionally, there is the implicit assumption of no energy leakage such that, in a stationary state, the rates of energy transfer and dissipation are equivalent (Gargett 1999). The LEM was first applied to glider data by Beaird et al. (2015) to study the variability of turbulent dissipation associated with the Nordic Sea inflows, and later by Evans et al. (2018) to investigate the seasonal variability of near surface mixing in the North Atlantic at 48°N. In both cases, glider-derived ε compared favorably with independent direct estimates from microstructure shear and acoustic Doppler current profiler (ADCP) velocity measurements, and indirectly with boundary-layer scalings.

Accepted for publication in *Journal of Physical Oceanography*. DOI 10.1175/JPO-D-19-0168.1.

Following Beaird et al. (2015) and Evans et al. (2018), the Ozmidov length $L_O = \sqrt{\varepsilon N^{-3}}$, where N is the buoyancy frequency, was used as the turbulent length scale (l). The turbulent velocity scale (u) was calculated as the root-mean-square of the vertical seawater velocity (w) fluctuations, $u \sim \sqrt{\langle w'^2 \rangle}$. With this, ε was computed as

$$\varepsilon = c_E N \langle w'^2 \rangle, \tag{2}$$

where c_E is an empirically-determined constant. Vertical water velocity was calculated by comparing the vertical profiling speed of the Seaglider, computed as the time-derivative of the pressure signal ($w_{\text{sg}} = \partial p / \partial t$), with an idealized model of the Seaglider flight (w_{hdm}) determined from the vertical density profile and the lift/drag/buoyancy characteristics of the Seaglider (Frajka-Williams et al. 2011): $w = w_{\text{sg}} - w_{\text{hdm}}$. Both $\langle w'^2 \rangle$ and N were calculated in half-overlapping 50 m bins so that an ε value was produced every 25 m, from 50 to 975 m. With a typical falling speed of 0.07-0.15 m s^{-1} and a sampling rate of 0.1 Hz, roughly 25–50 data-points were used for variance computation in each bin.

For the computation of velocity fluctuations (w'), it is important to remove the signal that does not correspond to dissipative turbulent motions, such as internal waves. The separation between the spectral bands of internal waves and turbulence is not always well defined in the ocean (D'Asaro and Lien 2000). Beaird et al. (2015) used a 4th order high-pass filter with a wavelength (λ_z) of 30 m to extract the turbulence signal, and argued that the final ε was insensitive to the choice of λ_z except for a multiplicative factor that could be reabsorbed in c_E, as long as $\lambda_z < 100$ m. Here, we follow the Beaird et al. (2015) approach to calculate w'. This procedure also has the advantage that w' variance is insensitive to inaccuracies in the glider flight model, which affect the w profile at low frequencies but not the small-scale fluctuations in w (Todd et al. 2017). Further,

Accepted for publication in *Journal of Physical Oceanography*. DOI 10.1175/JPO-D-19-0168.1.

high-frequency noise in the w signal due to the derivation of the pressure signal was removed using a 6-point Hamming window convolution.

Controlled changes in the glider roll or pitch affect the glider flight. Glider-controlled events compromise the assumption of steady flight, required for the application of the flight model and the calculation of w. Following Frajka-Williams et al. (2011), we removed data from the 25-s period following controlled maneuvers of the glider, and the gaps were filled by linear interpolation. Unfortunately, up until January 2018, when a change in the glider flight configuration was implemented, the control maneuvers were frequent, and the ε calculation was affected. Further, during this period, the vertical speed of Seaglider dives and climbs often exceeded > 0.2 m s^{-1} (and even > 0.4 m s^{-1} in the upper 100 m during dives). These relatively high vertical speeds affected the range of wavenumber fluctuations that could be resolved. To remove these data, 50-m segments were flagged as not valid when the number of data points affected by control maneuvers represented $> 10\%$ of the segment length, or when the profiling speed was outside the range $[0.08 - 0.18]$ m s^{-1}.

In order to calculate ε from Eq. 2, the constant c_E was determined by adjusting the glider estimates to ε calculated from tethered vertical microstructure profilers (VMPs) during the deployment and recovery cruises. A VMP measures the vertical velocity gradient (vertical shear) at the centimeter scale by means of two air-foil piezoelectric probes. The TKE dissipation rate is estimated from the variance of the vertical shear (assuming isotropic turbulence) as $\varepsilon = 7.5\nu\langle(\partial_z u)^2\rangle$, following Oakey (1982). As concomitant and co-located measurements of ε with the VMP and glider estimates were not available, we performed the optimization of c_E from log-averaged profiles (Figure 2). The log-averaged VMP profile was constructed with all the profiles collected during the two cruises. As VMP measurements were concentrated close to the continental margin (Figure 1), the comparison was restricted to the Seaglider profiles in water depths < 4500 m

Accepted for publication in *Journal of Physical Oceanography*. DOI 10.1175/JPO-D-19-0168.1.

(i.e. close to the shelf break). The calculation of c_E was performed using a least-squares minimization of the difference between the VMP and Seaglider profiles. To account for the variability between profiles, the difference at each depth was weighted by the sum of the standard deviations of both log-normal distributions. Figure 2 shows the agreement between the VMP and the adjusted Seaglider ε profiles. The obtained constant was $c_E = 0.055$, at the lower end of previous estimates (Moum 1996; Peters et al. 1995; Beaird et al. 2015; Evans et al. 2018).

3. Results

a. Overview of the glider mission

Figure 3 shows the oceanographic conditions during the glider mission between November 2017 and March 2018. Daily sea level anomalies interpolated onto the position of each glider profile were positive and > 10 cm until the end of January (Figure 3a). During this period, the altimetry indicated the presence of an anticyclonic eddy with maximum SLA of $\sim$25 cm, at 26°N, 75.5°W near the continental slope, with the eddy's southwestern rim flowing along the topography (Figure 4a,b). The interaction with a cyclonic feature located to the north of the anticyclone may be responsible for the intensification of the northeastward flow along the eddy's northern rim. Values of SLA close to or exceeding 20 cm at the glider sampling positions were found during three periods in mid-November (13–25 Nov), late December (11–30 Dec) and early January (1–14 Jan), indicating eddy influence at the sampling position. In January, the anticyclonic eddy started to drift to the northeast, as observed in the SLA shown in Figure 4c. By the end of the month, the anticyclone had left the sampling domain, and the SLA at the glider positions reduced to < 5 cm, reaching negative values due to the presence of a weaker cyclonic eddy by the end of February.

Accepted for publication in *Journal of Physical Oceanography*. DOI 10.1175/JPO-D-19-0168.1.

During this wintertime deployment, air-sea fluxes resulted in a persistent heat and buoyancy loss from the ocean, with a variable and smaller contribution by the net balance between evaporation and precipitation (Figure 3b). Due to this heat loss, mixed-layer temperature decreased steadily during the mission, and dropped more dramatically during intense cooling events around 10–14 December, 3–8 January and 25–29 January (Figure 3b,c). Except for a calm period during December, wind stress was variable but often exceeded 0.1 N m^{-2}, with daily peak values close to 0.3 N m^{-2} during the storms of 2–4 and 25–27 January.

The thermohaline imprint of the anticyclonic eddy in the potential temperature (θ) and S profiles recorded by the Seaglider appears as an upward deflection of the isotherms and isohalines above 200 db, and downward deflection below, for three periods highlighted in gray shading, coinciding with the positive altimetric anomalies (Figure 3c,d). The oxygen distribution, represented by apparent oxygen utilization (AOU), revealed the existence of a well-defined and highly oxygenated eddy core capped by the seasonal pycnocline, with AOU values (< 20 μmol kg^{-1}) that were up to about 30–40 μmol kg^{-1} lower than in the surrounding environment. From the AOU distribution (Figure 3e), the eddy core extended from the seasonal pynocline at $\sim$100 dbar to about 450 dbar. The eddy's influence was present in vertical displacements well below the eddy core, reaching the limits of the sampled vertical domain (1000 dbar).

The glider was piloted to span the region between the western side of the eddy and the eddy center as determined from near-real time altimetry, but was occasionally prevented from reaching the eddy center due to slow progress across the eddy's fast-flowing radial current. As outlined in Figure 4, the first glider transect ran from the north-northeastern rim of the eddy (13 November) to the western edge of the eddy (22 November). The closest position to the center of the eddy core was reached on the 16th of November (Figure 4b). At this time, the 18 °C isotherm reached a depth of 520 dbar, and the local SLA was 24 cm (Figure 3a,c). The second transect (11–30 December)

Accepted for publication in *Journal of Physical Oceanography*. DOI 10.1175/JPO-D-19-0168.1.

was conducted on the north-west rim of the eddy, between the eddy core and the bathymetric slope (Figure 4b). Due to slow progress, the glider was turned towards shore early, so that the maximum depth of the 18 °C isotherm was 500 m and the maximum SLA was 20 cm, indicating that the center of the eddy was not sampled during this transect (Figure 3a,c). Finally, during the third transect (1–13 January), the glider performed a clockwise loop across the eddy between its northwestern and southwestern flanks (Figure 4b). During this transect the maximum SLA was measured on the 7th of January (24 cm), when the 18 °C isotherm was at its deepest (530 db). This suggests that the eddy center was captured by this transect (Figure 3a,c).

Finally, Figure 3c shows the temporal evolution of the vertical distribution of TKE dissipation (ε) inferred from the Seaglider. Due to the piloting issues experienced during the initial two months of the mission (frequent glider control maneuvers), most of the ε data for this period were flagged as unreliable and are not displayed. In general, ε was maximum in the subsurface ocean down to the base of the pynocline at 200 dbar, with values close to 10^{-8} W kg^{-1} in the upper resolved bins. Below the subsurface layer, ε decreased to minimum values $< 10^{-9}$ W kg^{-1} within a depth range of 300-700 dbar, and relatively elevated below this depth. Reliable dissipation rates at the eddy center could be obtained during the third transect, revealing reduced dissipation ($< 5 \times 10^{-10}$ W kg^{-1}) within the core.

b. Dynamical properties of the eddy

The dynamical properties of the anticyclonic eddy are investigated with a focus on the third transect, during which the glider intercepted the eddy center and good-quality TKE dissipation rates were obtained. For this purpose, radial distributions of the different variables measured or estimated from the glider were produced by bin-averaging onto a regular grid ($\Delta r = 5$ km in the radial coordinate r, the horizontal distance from the glider profile to the estimated eddy center,

Accepted for publication in *Journal of Physical Oceanography*. DOI 10.1175/JPO-D-19-0168.1.

and $\Delta z = 5$ m in the vertical), using a Gaussian window with horizontal and vertical length-scales of 15 km and 5 m, respectively. The location of the eddy center was estimated with the glider high-resolution CTD measurements as follows. First, an initial guess for the position of the eddy core was determined as the location of the glider profile where the 18 °C isotherm displacement was maximum. r was defined as negative (positive) for the profiles collected before (after) the maximum displacement was observed. The interpolated potential density (ρ) distribution was then used to calculate the eddy azimuthal velocities from cyclogeostrophic balance (U_{cg}) (Joyce et al. 2013),

$$\left(f + \frac{2U_{cg}}{r}\right)\frac{\partial U_{cg}}{\partial r} = -\frac{g}{\rho}\frac{\partial \rho}{\partial r}. \tag{3}$$

Unfortunately, due to the occasional lack of GPS signal between profiles, absolute mean depth-integrated velocities could not be obtained from the dead-reckoning positions of the Seaglider, and the absolute cyclogeostrophic velocities were estimated using a level-of-no-motion at 1000 m. Finally, the radial distances were corrected by -16 km, so that $r = 0$ corresponded to the point where U_{cg} changed sign (see results in Figure 5).

The values of θ, S and potential density anomaly (σ_θ) were relatively uniform in the vertical within the eddy core (Figure 5a,b), which was weakly stratified with respect to the background (Figure 5c). The core had a radius of 60 km and extended between the main pycnocline ($\sigma_\theta = 25.5$ kg m^{-3}) and the 26.2 kg m^{-3} isopycnal (Figure 5). Mean properties in depth coordinates within the inner part of the eddy core ($r < 15$ km) and anomalies with respect to the background ($r > 80$ km) are shown in Figure 6. Mean θ, S and σ_θ in the eddy core (100–415 m) were 20.09 ± 0.50 °C, 36.69 ± 0.04 and 26.03 ± 0.10 kg m^{-3}, respectively (Figure 6a,b). The influence of the eddy in the thermohaline fields extended well below the core, with positive anomalies for θ, S and σ_θ of $+1.6$ °C, 0.6 and 0.25 kg m^{-3} as deep as 1000 m. Two narrow regions of positive buoyancy

Accepted for publication in *Journal of Physical Oceanography*. DOI 10.1175/JPO-D-19-0168.1.

frequency (N) anomaly were found at the top ($+0.005$ s^{-1}) and bottom ($+0.002$ s^{-1}), capping the eddy core in which the N anomaly was -0.018 ± 0.0008 s^{-1} ($\pm$ standard deviation) (Figure 6c).

Eddy cyclogeostrophic velocities were subsurface-intensified (Figure 5d). Azimuthal velocities (U_{cg}) were maximal at 130–230 m and at 60 km from the eddy center, reaching background values at $\sim$80 km from the eddy center . The velocity distribution was not axially symmetric, with maximum cyclogeostrophic velocities being 80% larger (50 cm s^{-1} vs. 29 cm s^{-1}) in the northwest ($r < 0$) compared to the southwest ($r > 0$) rim of the eddy. This asymmetry is consistent with the altimetry-derived surface velocities, which show an enhancement of the northeastward flow along the eastern part of the eddy near the continental margin (Figure 4). The mean azimuthal velocity between 130 and 230 m was proportional to the radial distance, $U_{cg} = \omega r$ (Figure 7), indicating that the core of the eddy was in approximate solid body rotation. The angular velocity calculated via a linear fit was $\omega = -8.31 \times 10^{-6}$ s^{-1}, corresponding to an orbital period ($T = 2\pi/\omega$) of 9 days. The local inertial frequency, f, was 6.61×10^{-5} s^{-1} ($T = 26$ hours), roughly ten times larger. The distribution of vertical relative vorticity was calculated as

$$\zeta = \frac{1}{r}\frac{\partial(rU)}{\partial r} \,, \tag{4}$$

assuming radial symmetry ($U = U(r,z)$). The eddy Rossby number, i.e. the ratio of vertical vorticity to planetary vorticity ($Ro = \zeta/f$), was on average -0.09 ± 0.06 within the eddy core (Figure 5e), consistent with the results from the linear fit ($Ro = \omega/f = -0.13$).

As a consequence of reduced stratification in the eddy core and negative relative vorticity of the flow, the eddy should present a negative anomaly of potential vorticity (PV). Ertel potential vorticity (q) is defined as

$$q = (2\vec{\Omega} + \vec{\nabla} \times \vec{u}) \cdot \vec{\nabla} b \,, \tag{5}$$

Accepted for publication in *Journal of Physical Oceanography*. DOI 10.1175/JPO-D-19-0168.1.

where $b=-g\rho/\rho_0$ is buoyancy with ρ the local potential density, ρ_0 a reference density and Ω is the Earth's rotation rate. In our dataset, at the scales ($\Delta r \approx 15$ km) resolved by the smoothed distributions across the eddy, the horizontal terms ($q_H = 2\Omega \cos\phi + (\partial_y w - \partial_z v)\partial b_x + (\partial_z u - \partial_y w) b_y$, where ϕ is latitude) were at least an order of magnitude smaller than the vertical, and we calculated q as $q \approx q_V = (f+\zeta)N^2$. Within the eddy core ($r < 15$ km, 100–415 m depth range), $q \approx 0.5\times10^{-9}$ s^{-3}, while outside the eddy ($r > 80$ km), q ranged from 1.5×10^{-9} s^{-3} to 7×10^{-9} s^{-3}, in the same depth interval. Therefore, the negative q anomalies within the eddy core were of about 1×10^{-9} s^{-3}, and reached 4.5×10^{-9} s^{-3} at the top of the core at 115 m (Figure 6e).

c. Energy content and dissipation

The energetics of the eddy were studied by calculating its available potential energy (APE) and kinetic energy (KE) assuming radial symmetry (Hebert 1988), as

$$APE = \pi \int_{-R}^{R}\int_{-H}^{0} gz(\rho_{ref}(z)-\rho(r,z))r\,\mathrm{d}r\,,\mathrm{dz}\,, \quad (6)$$

$$KE = 0.5\pi \int_{-R}^{R}\int_{-H}^{0} \rho(r,z)U(r,z)^2 r\,\mathrm{d}r\,,\mathrm{dz}\,, \quad (7)$$

where H is the maximum depth (1000 m), and ρ_{ref} is the mean potential density profile outside the eddy influence ($r > 80$ km, Figure 6c). The horizontal integration was carried out to $R = 80$ km. The eddy contained considerably more APE (4.38×10^{15} J) than KE (3.56×10^{14} J), and the eddy Burger number (D'Asaro 1988) was small, $B_E = KE/APE = 0.081$. A different formulation of the Burger number can be constructed based on the length-scale Burger number ($B_L = N^2L_z^2/f^2L_x^2$, where L_x and L_z are the vertical and horizontal dimensions of the eddy) as $B_E \approx B_L/(1+Ro)$ (Prater and Sanford 1994). Using $L_z = 500$ m, $L_x = 120$ km, and a background $N^2 = 2.5\times10^{-5}$ s^{-2}, the length scale-based B_E estimate is 0.088, in good agreement with B_E obtained from the energy ratio.

Accepted for publication in *Journal of Physical Oceanography*. DOI 10.1175/JPO-D-19-0168.1.

Finally, the values and distribution of TKE dissipation within the eddy were derived from the Seaglider measurements using the large-eddy method (Figure 5f). Consistent with the general picture during the mission, ε was elevated in the upper 200 m, including the mixed-layer and the upper pycnocline. In the near-surface layers, an asymmetry in dissipation rates was observed between the first (northwest) and second (southwest) parts of the transect, with ε decreasing by almost an order of magnitude from $1-2\times10^{-8}$ W kg^{-1} to $\sim3\times10^{-9}$ W kg^{-1}. We attribute these differences to the strong atmospheric energy input during the first period rather than to spatial variability (Figure 3b). Dissipation rates were minimal (on average 5×10^{-10} W kg^{-1} between 200–400 m) within the eddy core (Figure 5f), reaching values as low as 2×10^{-10} W kg^{-1} in individual profiles. At the same depth, but outside the eddy core, ε reached values of $\sim10^{-9}$ W kg^{-1}, similar to the mean values in lower layers (400–1000 m). In this deeper vertical range, dissipation was also slightly larger at northwest ($\varepsilon\approx1\times10^{-9}$ W kg^{-1}) compared to the southwest ($\varepsilon\approx7\times10^{-10}$ W kg^{-1}) rim of the eddy. However, larger dissipation rates exceeding 10^{-9} W kg^{-1} were found in the central part of the section ($-50<r<20$ km).

d. Eddy-internal wave interactions as drivers of turbulent dissipation

A closer look at the vertical structure of the vertical water velocity (w) across the anticyclonic eddy shows that relatively elevated (reduced) levels of energy dissipation below (inside) the eddy core coincided with the presence of wave-like structures (Figure 8). This figure displays two profiles of w obtained with the glider, one collected 10 km to the northwest of the eddy center on the 7th of January, and a second collected 50 km to the southwest of the eddy center on the 10th of January. The first profile exhibits a quasi-periodic structure with depth (vertical wavelength $\lambda_z\approx200$ m) occupying the water column between 200 and 1000 m with an amplitude of 0.01 m s^{-1} and coinciding with elevated levels of turbulent dissipation. In the second profile, the wave-

Accepted for publication in *Journal of Physical Oceanography*. DOI 10.1175/JPO-D-19-0168.1.

like structure was absent, the velocity amplitudes were much smaller and the levels of dissipation were lower.

In order to confirm the presence of the wave-like structures and study their characteristics, profiles of density perturbation (ρ') were computed as potential density anomaly relative to a smooth density profile calculated using the Bray and Fofonoff (1981) adiabatic leveling algorithm (Figure 8). Briefly, isopycnal displacements (δz) were calculated by comparing the measured specific volume at a given depth z ($\alpha(z) = 1/\rho(z)$) with the value corresponding to a smoothed $\overline{\alpha}$ profile, obtained by fitting a 5-degree polynomial against depth over a 400 m interval centered at z. A smoothed $\overline{N}^2$ profile was calculated then as $\overline{N}^2 = -g\rho_0(dz/d\overline{\alpha})^{-1}$, where ρ_0 is the mean density over the 400 m interval, and the density perturbations were computed as $\rho'(z) = \rho_0/g\overline{N}^2\delta z$. Finally, hydrostatic pressure perturbation (p') was calculated as

$$p' = \int_z^0 \rho' g\,\mathrm{d}\hat{z} - \frac{1}{H}\int_{-H}^0 \int_z^0 \rho' g\,\mathrm{d}\hat{z}\,\mathrm{d}z \quad (8)$$

where the second term on the right-hand side is used to remove the barotropic pressure perturbation. Both ρ' and p' exhibit wave-like structures on the high-dissipation profile, which are absent on the low-dissipation profile (Figure 8). The vertical energy flux associated with an internal wave is given by the co-variance of the vertical velocity and pressure perturbations, $F_z = \langle w'p' \rangle$. Therefore, a positive correlation between w' and p' indicates upward energy propagation. Figure 8 shows the correlation coefficients between w' and p' ($R_\mathrm{c}^2 = \langle w'p' \rangle / \sqrt{\langle w'^2 \rangle \langle p'^2 \rangle}$). The energetic wave-like structure is associated with a positive correlation between both variables ($R_\mathrm{c}^2 = 0.6$), which reinforces confidence in the observation and indicates that the structure may be upward-propagating. In the low-dissipation profile, the coherence between both variables was poor ($R_\mathrm{c}^2 = 0.1$).

These results suggest that the observed patterns of dissipation may be related to internal waves interacting with the anticyclonic eddy. The evolution of vertical strain variance (γ_z) during the

Accepted for publication in *Journal of Physical Oceanography*. DOI 10.1175/JPO-D-19-0168.1.

glider survey illustrates the generality of this observation (Figure 9a). Vertical strain is associated with the vertical motions induced by internal waves, and was calculated as $\gamma_z = (N^2 - \overline{N}^2)/\overline{N}^2$, using the Bray and Fofonoff (1981) procedure. The variance of vertical strain computed between 200 and 1000 m was enhanced when the glider sampled in the vicinity of the anticyclonic eddy core (purple, green and red shaded areas), and regularly peaked at the location of the maximum isopynal displacement (close to the eddy core). Other periods of enhanced γ_z occurred when the glider was sampling close to the continental shelf, particularly in instances of northward flow (e.g., 25 November–4 December). Clément et al. (2016) showed that the northward flow of anticyclonic eddies impinging on topography in our study area generates small-scale internal waves over the 600 m isobath, which we may be capturing with our glider observations.

Vertical wavenumber spectra of vertical velocity and strain are shown for five selected periods (eddy transect 1, eddy transect 2, eddy transect 3 northwest, eddy transect 3 southwest, and a reference period with no eddy) in Figure 9b,c. During the glider transects that intersect the eddy, levels of strain variance were enhanced, at least for part of the sections, with respect to the non-eddy period, characterized by strain variance closer to the background oceanic value (Garrett and Munk 1979). All the transects show a peak of γ_z variance at a wavelength of $\lambda_z = 90 - 250$ m, which was absent during the reference period. During transects 1 and 3, when the eddy core was clearly intercepted, the strain variance enhancement extended across all resolved wavelengths, reaching scales of $\mathcal{O}(10)$ m. As previously mentioned, vertical water velocity could not be calculated for transects 1 and 2, but the w spectrum for transect 3 showed a clear enhancement at all wavelengths, especially for $\mathcal{O}(100)$ m. The asymmetry in the internal wave characteristics during transect 3 is also illustrated by Figure 9b,c. While both w and γ_z variance levels were enhanced during the first part of the transect (northwest flank and center of the eddy), they were close to background levels during the second part (southwest flank).

Accepted for publication in *Journal of Physical Oceanography*. DOI 10.1175/JPO-D-19-0168.1.

e. Ray-tracing diagnosis

In order to understand the patterns of turbulent dissipation in the eddy, we use a heuristic ray-tracing calculation (e.g., Lighthill 1978; Olbers 1981; Whitt and Thomas 2013) to diagnose the origin and characteristics of the observed internal waves and their evolution due to interaction with the eddy. The propagation of internal wave packets, and the changes in their properties along a ray path, are determined using background stratification and velocity fields. For linear waves in a slowly varying background flow (Wentzel-Kramers-Brillouin, WKB, approximation) the equations governing the temporal evolution (d/dt) of the position ($\vec{x} = (x, y, z)$) and wavevector ($\vec{k} = (k, l, m)$) of an internal wave group (and its energy) (Olbers 1981) are

$$\frac{d\vec{x}}{dt} = \nabla_{\vec{k}} \omega_e \ , \tag{9}$$

$$\frac{d\vec{k}}{dt} = -\nabla_{\vec{x}} \omega_e \ , \tag{10}$$

where $\nabla_{\vec{k}}$ and $\nabla_{\vec{x}}$ are the gradients in wavevector and physical space, respectively, and ω_e is the frequency of the wave for an external observer in a fixed reference frame, or Eulerian frequency. In a steady background flow, the Eulerian frequency is conserved along the ray propagation path, and is related to the intrinsic frequency of the wave (ω) through Doppler-shifting by the mean flow ($\vec{U}$),

$$\omega_e = \omega - \vec{k} \cdot \vec{U} \ . \tag{11}$$

An extreme situation occurs when the velocity of the background flow equals the wave propagation velocity and the wave enters a critical layer: the Doppler effect is such that ω asymptotically approaches f and the propagation of the wave is arrested, and the wave transfers its energy mainly toward dissipation scales (Munk 1981). The intrinsic frequency in Eq. 11 is linked to the wavevector and the background stratification (and flow shear) through the dispersion relation. Kunze (1985) derived an expression for the dispersion relation of low-frequency waves ($\omega \ll N$)

Accepted for publication in *Journal of Physical Oceanography*. DOI 10.1175/JPO-D-19-0168.1.

propagating in weakly baroclinic and weakly sheared ($Ro \ll 1$, $Ri = S^2/N^2 \gg 1$) flows:

$$\omega = f_{eff} + \frac{N^2(k^2+l^2)}{2fm^2} + \frac{1}{m}\left(\frac{\partial U_x}{\partial z}l - \frac{\partial U_y}{\partial z}m\right). \tag{12}$$

In this derivation, the mean-flow shear terms are included in the dispersion relation, allowing the wave to interact with the background flow shear. The shear terms determine flow vorticity, and thus modify the low-frequency limit for wave propagation ($f_{eff} \approx f + \zeta/2$). Those terms are relevant notably for near-inertial waves ($\omega \approx f$). In this context, waves produced within a region of $f_{eff} < f$ are trapped, and can also enter a critical layer when propagating away from it (e.g., Fer et al. 2018). Although less restrictive solutions now exist for this problem (Mooers 1975; Whitt and Thomas 2013), in which the effects of baroclinicity on wave propagation are accounted for, in the context of our observations, the requirements for the Kunze (1985) approximation are met ($Ro \approx 0.1$, $Ri \gtrsim 10$), so we chose to proceed with this approximation.

The numerical ray-tracing experiments were forced with three-dimensional fields of N and $\vec{U}$ reconstructed from the glider-derived eddy observations during the third transect. To construct the three dimensional fields, perfect radial symmetry was assumed for simplicity, and the N and U profiles for negative and positive values of the r coordinate in Figure 5 were merged. We followed the approach of initially placing waves with the observed properties at the position of the observations and running the simulation backwards in time, in order to track the evolution of each wave when interacting with the eddy, and infer the original position and properties of that wave. Our observations provided a rough estimate of initial position and vertical wavelength of the wave ($\lambda_z = 100 - 300$ m), related to the vertical wavenumber through $k_z = 2\pi/\lambda_z$. To initialize a wave, either the frequency or the horizontal wavenumber are required, but neither were known. As critical layer absorption is a plausible mechanism leading to reduction of the wave dimensions and transfer of energy to dissipation, we opted to set the initial intrinsic frequency to $\omega \approx f$,

Accepted for publication in *Journal of Physical Oceanography*. DOI 10.1175/JPO-D-19-0168.1.

and infer the original frequency of the wave using the backward simulations. The choice of low (near-inertial) frequency implies a slow vertical propagation speed, which is consistent with our observations of coherent structures in w and p' for the duration of a glider profile ($\sim$3 hours).

An example of an experiment carried out with an upward-propagating wave with initial $\lambda_z = 150$ m and $\omega = 1.05f$ located at 300 m depth and 30 km away from the eddy core at $t = 0$ is shown in Figure 10. As the Doppler shift is given by the dot product of the wave and flow velocity vectors (Eq. 11), the initial wave propagation direction was set parallel to the local flow to maximize the Doppler effect. The experiment indicated that, as the wave entered the eddy, the propagation of the wave stalled, the intrinsic frequency asymptotically approached f, and the wavelength shrunk from its original value of $\lambda_z = 382$ m to 150 m. The simulation revealed that the original frequency of the wave was very close to the semi-diurnal (period of 12.42 hours) tidal frequency ($\mathrm{M}_2 = 14 \times 10^{-5}$ s^{-1} or $\mathrm{M}_2 = 2.12f$), suggesting that a plausible explanation for our observations is that relatively short wavelength internal tides encounter critical layers in the eddy shear. As the inferred unperturbed wave parameters are sensitive to the choice of initial conditions, a 1000-simulation Monte Carlo experiment with varying initial conditions was performed ($x \in [0, 50]$ km, $z \in [300, 500]$ m, $\omega \in [1.05f, 1.50f]$, $\lambda_z \in [100, 300]$ m) to assess the statistical significance of this result. This experiment determined that the original wave would have an intrinsic frequency $\omega = 13.9 \pm 4.1 \times 10^{-5}$ s^{-1} ($\pm$ standard deviation) (corresponding to a period of 12.58 ± 3.80 hours), and vertical and horizontal wavelengths of 283 ± 122 m and 13 ± 6 km, respectively.

The possibility of near-inertial waves (NIWs) being trapped by the eddy and that the waves' energy may be focused below the eddy core (e.g., Kunze 1985; Kunze et al. 1995; Lonergan and White 1997; Fer et al. 2018; Zhang et al. 2018) was explored in subsequent ray-tracing experiments. Negative vorticity in the eddy can enhance the vertical propagation of NIWs due to the reduction of the effective minimum frequency for internal wave propagation (f_{eff}), and allows

Accepted for publication in *Journal of Physical Oceanography*. DOI 10.1175/JPO-D-19-0168.1.

the propagation of near-inertial waves with $f_{eff} < \omega < f$ produced and trapped within the eddy. Accordingly, we performed an experiment with a near-inertial wave with $\omega = 0.95f$, to represent a NIW generated within the eddy (Figure 11). The wave was initialized below the eddy core ($z = 500$ m) near the eddy center ($x = -10$ km), where the elevated dissipation and wave-like structures were observed, with a downward vertical group propagation. As near-inertial energy capture does not require Doppler shift, this term was initially set to zero by forcing the propagation direction to be perpendicular to the eddy flow (i.e. directed towards the eddy center). The backward calculation showed that the wave could propagate from the surface to the base of the eddy core in a time-span of 40 days (or 25 days from the pycnocline). The downward propagation was inhibited at the pycnocline by large stratification, but vertical wavenumber was again reduced (larger λ_z) within the eddy core (radial distance $R < 30$ km), enhancing vertical propagation, due to negative flow vorticity and vertical stratification. The vertical and horizontal propagation was also inhibited when the wave approached the horizontal boundaries of the eddy core (where $f_{eff} \approx f$), and two turning points (horizontal wavenumbers $k, l = 0$, and wave speed $c = 0$) were inferred at $R \approx 45$ km, indicating that wave energy was trapped by the eddy. According to this set of calculations, the original NIW had a vertical (horizontal) wavelength of 680 m (96 km) at the surface, which drastically reduced to 150 m (18.4 km) at the base of the eddy core (as set by the initial conditions). The wave experienced an increase in m (reduction in λ_z) and a stalling of its vertical and horizontal progression upon reaching the base of the eddy core, indicating a focusing of wave energy and a critical layer as ω approached f_{eff}.

4. Discussion and Conclusions

An anticylonic eddy was observed in situ at the western boundary of the North Atlantic subtropical gyre off the Great Abaco Island, Bahamas, during a four-month glider survey (November

Accepted for publication in *Journal of Physical Oceanography*. DOI 10.1175/JPO-D-19-0168.1.

2017 to February 2018). The eddy had a lens-like core identified as a thermostad, halostad and pycnostad capped by the seasonal pycnocline and extending down to 450 m. Potential vorticity (PV) and apparent oxygen utilization were reduced within the core, and the cyclogeostrophic circulation around the eddy was subsurface-intensified. These characteristics suggest that the observed structure was an intrathermocline eddy or mode water eddy (Dugan et al. 1982; McWilliams 1985; McGillicuddy et al. 2007; McGillicuddy 2015; Schütte et al. 2016). Mode water eddies are often associated with western boundary currents, and are formed by subduction or capping of a recently ventilated mixed-layer (Hanawa and Talley 2001; Speer and Forget 2013). The body of mode water is trapped within the closed contours of PV of the eddy core and transported far away from the source, representing a significant pathway for the spreading of mode waters (Zhang et al. 2017; Xu et al. 2016). In the western North Atlantic, mode water eddies carrying western North Atlantic subtropical mode water (or Eighteen Degree Water, EDW, $\theta \approx 18$ °C, $S = 36.5$, $\sigma_\theta = 26.5$ kg m^{-3}), formed in the area south of the Gulf Stream, are a common feature. Lagrangian measurements with floats have shown that they can drift southwestward, reaching the western boundary of the North Atlantic subtropical gyre at the latitude of our observations (Fratantoni et al. 2013).

Insights on the water-mass characteristics and origin of the eddy can be obtained from its thermohaline properties (Figure 12). The θ-S diagram shows that the water-mass contained in the eddy core was generally cooler and saltier along isopycnals, compared to the background. The inner core of relatively well ventilated water (AOU ≈ 15 μmol kg^{-1}) was contained between 26.0 and 26.1 kg m^{-3} and had a uniform salinity of 36.65 with $\theta = 19.5-20.2$ °C, being saltier, warmer and lighter than the canonical EDW (Hanawa and Talley 2001). Following Zhang et al. (2015) and Li et al. (2017), we used the climatological salinity and AOU distribution on the $\sigma_\theta \approx 26.05$ kg m^{-3} surface, derived from the World Ocean Atlas 2013 (Locarnini et al. 2013; Zweng et al. 2013; Garcia et al. 2013), to estimate a potential generation region of the eddy. A broad area was

Accepted for publication in *Journal of Physical Oceanography*. DOI 10.1175/JPO-D-19-0168.1.

identified as possible source of the eddy to the northwest of the observation site at 50 – 70°W, 22 – 32°N. In this area, salinity and AOU at the 26.05 kg m^{-3} isopycnal were 36.6-36.7 and 0–15 μmol kg^{-1}, respectively (because AOU increases over time, it can be assumed to be as low as 0 μmol kg^{-1} at the time of formation). The potential formation area is located to the south of the main EDW pool at ∼55°W, 35°N (Forget et al. 2011), which might explain the differences in thermohaline properties.

From a dynamical perspective, the observed anticyclone was relatively large (with a radius of 60 km between the eddy center and the velocity maximum) and energetic. The eddy radius was larger than the internal deformation radius ($R_d = NH/f \approx 33$ km, where $H \approx 500$ m and $N \approx 4.5 \times 10^{-3}$ s^{-1}), which is usually a good approximation for the size of intratermocline submesoscale eddies (Dewar and Meng 1995; Zhang et al. 2015). The eddy was also 30% larger than the first local baroclinic radius of deformation, $R_d = c_i/|f| = 46$ km, where $c_i = 2.9$ m s^{-1} is the phase-speed of the first baroclinic mode obtained by solving the Sturm-Liouville equation for the local mean stratification profile (Gill 1982; Chelton et al. 1998). The Rossby ($Ro \approx -0.1$) and Burger ($Bu \approx 0.1$) numbers were modest, and the eddy was characterized by a strong potential energy anomaly relative to kinetic energy. These properties resemble those of mesoscale eddies observed in the ocean's most energetic regions, such as western boundary currents like the Gulf Stream and Loop current (e.g., Olson et al. 1985; Meunier et al. 2018a). They differ, however, from a common type of intrathermocline eddies, often termed submesoscale coherent vortices (SCVs) (McWilliams 1985), which are usually much smaller (5 - 20 km), and present larger *Ro* and *Bu* (McWilliams 1985; Reverdin et al. 2009; Bosse et al. 2015; Meunier et al. 2018b).

Using glider-derived vertical water velocities we estimated rates of TKE dissipation, tuned against microstructure profiler measurements, inside and around the eddy. From the spatial survey accomplished by the glider, we identified a relatively quiescent eddy core with enhanced dissipa-

Accepted for publication in *Journal of Physical Oceanography*. DOI 10.1175/JPO-D-19-0168.1.

tion beneath. Several previous studies have reported turbulent dissipation rates in intrathermocline eddies in diverse environments. Lueck and Osborn (1986) reported a strikingly similar pattern of TKE dissipation suppression (enhancement) within (below) the core of a Gulf stream warm ring with similar characteristics and dimensions to those described here. Using tracer release experiments in the Gulf Stream area, Ledwell et al. (2008) measured elevated values of diapycnal diffusivity in a mode water eddy. In the Southern Ocean, Sheen et al. (2015) documented a similar distribution of TKE dissipation in a deep low-PV anticyclonic eddy located at 2000 m depth in Drake Passage. Forryan et al. (2012) reported low values of dissipation in the core of a Western Mediterranean intermediate mode water anticyclonic eddy, located below the pycnocline (100–300 m) in the Alborán Sea, with some hints of elevated dissipation at the base of the eddy core. Finally, recent microstructure observations of the permanent anticyclonic Lofoten basin eddy in the Nordic Seas revealed low dissipation levels in the fast-rotating, highly-baroclinic ($Ro \approx -f$, $Ri \approx 1$), low-PV eddy core, with enhanced dissipation at the base of the core (Fer et al. 2018). Thus, the suppression of dissipation within the low-PV cores of intrathermocline anticyclonic eddies, and the enhancement of dissipation below, appears to be a common feature of these structures. The reason for the suppression of dissipation in the eddy core could be related to the dispersion relation dictating an increase of the wave dimensions due to reduced stratification and negative vorticity (Eq. 12) (Kunze 1985). The increase of wave dimensions causes a reduction in wave shear, which results in weaker energy transfer to dissipation scales through wave-wave interactions (Henyey et al. 1986; Gregg 1989; MacKinnon and Gregg 2003). In fact, Gregg and Sanford (1988), showed that internal wave-driven dissipation in the ocean thermocline scales with a positive power of the buoyancy frequency. Furthermore, high-frequency waves can potentially be reflected away from the weakly stratified eddy core (Sheen et al. 2015).

Accepted for publication in *Journal of Physical Oceanography*. DOI 10.1175/JPO-D-19-0168.1.

Past studies have argued that internal wave-eddy interactions drive enhanced turbulent dissipation (Lueck and Osborn 1986; Ledwell et al. 2008; Sheen et al. 2015; Fer et al. 2018), while the trapping of near-inertial energy due to the reduction of the effective resonance frequency in anticyclonic eddies was frequently invoked as the underlying mechanism. For example, Fer et al. (2018) used ray-tracing experiments based on the dispersion relation of Whitt and Thomas (2013), as required for the high-*Ro* low-*Ri* Lofoten eddy, to show how near-inertial energy was trapped and focused at the base of the eddy core. An exception is provided by Sheen et al. (2015), where the authors neglected the rotational effects in their ray-tracing simulations and demonstrated that the reduced stratification and enhanced shear within the eddy core could explain the distribution of TKE dissipation by reflecting some waves at the boundaries of the eddy core while driving critical layer situations for other waves, above and below the core. Another notable exception is found in Zhang et al. (2019), who quantified turbulent mixing with a *Ri*-based parameterization in an intrathermocline anticyclonic eddy and found enhanced diffusivities surrounding the eddy core. However, this dissipation was induced by sub-inertial mesoscale shear, while the downward propagation of near-inertial shear was inhibited by the eddy. Zhang et al. (2019) invoked the linear NIW propagation equations developed by Kunze (1985) to argue that the eddy stratification and shear caused NIW reflection and confinement in the surface layer (Byun et al. 2010).

To investigate potential mechanisms responsible for our observed pattern of dissipation, we used ray-tracing simulations, in which we chose to focus on low-frequency internal waves. The interaction of higher-frequency waves with the eddy, leading for example to reflection on the eddy core (e.g., Sheen et al. 2015), could also have contributed to the observed dissipation pattern. Two potential interaction mechanisms involving low-frequency waves were identified: (i) NIW trapping in the negative vorticity of the eddy, or (ii) small-scale internal tides encountering a critical layer in the eddy's sheared flow. In the first interpretation, NIWs generated in the eddy would be

Accepted for publication in *Journal of Physical Oceanography*. DOI 10.1175/JPO-D-19-0168.1.

trapped within the region of negative relative vorticity. Together with reduced vorticity (contrary to the conclusions of Zhang et al. (2019)), the reduced stratification in the eddy core would play an important role in enhancing the downward propagation of NIW energy within the eddy. This NIW energy would be focused towards the base of the eddy core, where our calculations indicate that waves with $\omega < f$ enter a critical layer situation. In the second interpretation, relatively small-scale ($\lambda_z \approx 300--400$ m) internal tides (ITs) with a semidiurnal M_2 frequency would propagate upwards across the eddy, encountering a critical layer in the eddy shear.

Examining the spatial distribution of turbulent dissipation and strain variance, the temporal relationship between dissipation and wind forcing, and the direction of propagation of the internal waves may provide some clues in support of one or the other mechanism. A critical layer for ITs would be favored at the location of the maximum vertical shear, i.e. below the velocity maximum, while NIW energy focusing would occur towards the base and center of the eddy core. The distribution of strain variance along the different transects across the eddy shows a peak at the location of the maximum isothermal displacement, consistent with the focusing of NIW energy (Figure 9). If the NIW mechanism is responsible for the observed dissipation, then the dissipation should be particularly elevated during periods of high winds, with possibly some delay of $\sim$10 days, required for the vertical energy propagation. Indeed, the first and third transects corresponded to high-wind and high-dissipation periods (Figure 3). However, during the second transect, elevated strain variance was still observed in spite of a prolonged calm period, while during the second half of the third transect, low dissipation was observed in spite of high winds. Despite this inconsistency, which would hint at a more permanent source of waves like ITs, a recent study described the trapping of NIW energy in a mesoscale eddy during a period of weak wind forcing (Martínez-Marrero et al. 2019). Finally, inspection of vertical velocity and pressure perturbations revealed that they are in phase when the dissipation is elevated and the wave-like structures in w and pressure per-

Accepted for publication in *Journal of Physical Oceanography*. DOI 10.1175/JPO-D-19-0168.1.

turbation are apparent (Figure 9). The phase difference suggests an upward-propagating feature, supporting the IT hypothesis in preference to the NIW interpretation. Nonetheless, other profiles of wave properties show similar wave-like structures with poor coherence, or even suggesting downward propagation (not shown). Further, in a critical layer situation, the vertical propagation of wave energy may not be well-defined.

A further significant feature in our dataset was an observed asymmetry between the northwest and southwest flanks of the eddy (transects 1 and 3, Fig. 9). This asymmetry could be explained by the interaction between small-scale ITs and the eddy, governed by the Doppler shift term in the dispersion relation. A semi-analytical model for barotropic-to-baroclinic tidal conversion (Vic et al. 2019) applied to our study region indicates that the continental shelf at the region's western boundary is a source of internal tides of different modes that propagate eastward towards the ocean interior (Figure 13), possibly interacting with the abundant mesoscale eddies in this region (Clément et al. 2016). The Doppler shift effect underpinning the generation of a critical layer situation depends on the dot product between the wavevector ($\vec{k}$, set by the wave propagation direction) and the background flow velocity ($\vec{U}$) (Eq. 11). A shift towards low frequencies and, accordingly, a critical layer situation is only possible when $\vec{k} \cdot \vec{U} > 0$, that is, when the wave propagates in the flow direction. In our observations, such a situation is only found in the northern rim of the eddy, where the background flow and wave propagation are eastward. In the case of wave propagation directed perpendicular to the center of the eddy (in the western rim), $\vec{k} \cdot U$ is zero and no frequency shift is expected. In the eddy's southern flank, where $\vec{k} \cdot U < 0$, one would expect an expansion of the vertical structure of the wave and an enhancement of the vertical propagation, such that a shrinking of the wave and a pathway to dissipation is not expected. This was confirmed in ray-tracing simulations (not shown). Finally, Figure 13 shows that internal tide generation is stronger in the shelf to the north of the Bahamas, which may also explain the observed asymmetry.

Accepted for publication in *Journal of Physical Oceanography*. DOI 10.1175/JPO-D-19-0168.1.

In summary, together with potential interactions with high-frequency internal waves, two mechanisms may explain the observed dissipation patterns in the anticyclonic eddy observed here: NIW trapping by the reduced relative vorticity within an anticyclonic eddy, or ITs encountering a critical layer in the eddy shear. These observations highlight a potentially important sink of internal wave energy in the ocean via wave-eddy interactions, with the two mechanisms likely having distinct influences on large-scale patterns of dissipation. Global deep-ocean estimates of turbulent dissipation from Argo profiling floats suggest that mesoscale eddies may significantly enhance turbulent mixing by NIWs within the upper 2000 m of the water column, particularly within anticyclonic eddies (Whalen et al. 2018). However, Argo floats are limited in their ability to sample full ocean basins, in that they do not routinely measure on continental slopes (i.e. in waters shallower than 2000 m). Our observations are in an anticyclonic eddy over the continental slope, and thereby provide a high-resolution view of turbulent dissipation that is mostly consistent with trapping of NIWs.

At any rate, the balance of evidence here supports an alternate hypothesis for turbulent dissipation in mesoscale eddies. ITs generated at the boundary may propagate into the mesoscale eddy and encounter a critical layer situation there, leading to enhanced local dissipation of tides. ITs are one of the main sources of mixing power in the ocean interior (Munk and Wunsch 1998), yet the spatial distribution of IT breaking is not well understood. A prominent source of uncertainty is the fate of small-scale (high-mode, typically mode $> 3-4$) ITs (MacKinnon et al. 2017; de Lavergne et al. 2019; Vic et al. 2019). Parameterizations of internal tide mixing commonly assume that a small fraction of the IT energy is imparted to high-modes that dissipate within the source region (St. Laurent and Garrett 2002). A recent study has challenged this paradigm by showing that the fraction of local IT dissipation could be highly variable and much higher than previously thought (Vic et al. 2019). Local IT dissipation is thought to be controlled by poorly constrained, weakly

Accepted for publication in *Journal of Physical Oceanography*. DOI 10.1175/JPO-D-19-0168.1.

non-linear wave-wave interactions (Eden and Olbers 2014). Our results put forward a novel mechanism by which mesoscale eddies, ubiquitous in the world's oceans could act as a leaky wall to ITs generated on continental slopes. Whether or not an IT permeates through this wall depends on the relative orientation of the eddy flow and the IT's wave vector. From our ray-tracing simulations, the propagation of an IT is stalled by the eddy flow when the flow speed and wave group speed are of similar magnitude. Mesoscale eddies have typical velocities of $0.5-1$ m s^{-1}, overlapping with the characteristic range of phase speeds for ITs.

Using high-resolution observations from a 4-month glider transect, we have documented elevated turbulent dissipation in an anticyclonic eddy over the continental slope east of the Bahamas (26.5°N) at the western boundary of the Atlantic. These observations highlight the likely importance of mesoscale eddies in shaping open-ocean dissipation. Due to the relatively coarse resolution of climate-scale ocean models, the influence of mesoscale features on dissipation cannot be routinely simulated, and models instead rely on parameterizations for dissipation and mixing, which has been shown to critically influence the mean structure of the large-scale ocean circulation (Danabasoglu et al. 2014). The two mechanisms highlighted here will have distinct impacts on the large-scale patterns of dissipation, with the IT mechanism enhancing dissipation near continental slopes, and the NIW mechanism occurring basin-wide. Although we cannot conclusively determine which of these two mechanisms is active here (due to the short data record and uncertainty in the spatial geometry of the eddy), our study highlights the potential of sustained glider observations in uncovering the drivers of turbulent dissipation near topographic boundaries, which are difficult to sample with other technologies.

Acknowledgments. The MerMEED project is funded by the U.K. Natural Environment Research Council (NE/N001745/1). B. Fernández-Castro was supported by a Juan de La Cierva-Formación

Accepted for publication in *Journal of Physical Oceanography*. DOI 10.1175/JPO-D-19-0168.1.

postdoctoral fellowship (FJCI-641 2015-25712) and a José Castillejo travel grant (CAS18/00017) by the Spanish Government. A. Naveira-Garabato was supported by the Royal Society and the Wolfson Foundation. We acknowledge the crew of the Walton Smith and the glider pilots from Marine Autonomous Robotic Systems at the National Oceanography Centre Southampton. The glider and microstructure data are available on-line at the British Oceanographic Data Centre (https://www.bodc.ac.uk/).

References

Alford, M. H., 2003: Redistribution of energy available for ocean mixing by long-range propagation of internal waves. *Nature*, **423**, 159–163, doi:10.1038/nature01591.1.

Alford, M. H., J. A. MacKinnon, H. L. Simmons, and J. D. Nash, 2016: Near-Inertial Internal Gravity Waves in the Ocean. *Annual review of Marine Science*, **8**, 95–123, doi:10.1146/annurev-marine-010814-015746.

Beaird, N., I. Fer, P. B. Rhines, and C. C. Eriksen, 2015: Dissipation of turbulent kinetic energy inferred from seagliders: an application to the Eastern Nordic Seas overflow. *Journal of Physical Oceanography*, **42**, 2268–2282, doi:10.1175/JPO-D-12-094.1.

Bosse, A., P. Testor, L. Mortier, L. Prieur, V. Taillandier, F. D'Ortenzio, and L. Coppola, 2015: Spreading of Levantine Intermediate Waters by submesoscale coherent vortices in the northwestern Mediterranean Sea as observed with gliders. *J. Geophys. Res.*, **120**, 1599–1622, doi:10.1002/2014JC010263.Received.

Bray, N. A., and N. P. Fofonoff, 1981: Available potential energy for MODE eddies. *Journal of Physical Oceanography*, **11 (1)**, 30–47, doi:10.1175/1520-0485(1981)011⟨0030:APEFME⟩2.0.CO;2.

Accepted for publication in *Journal of Physical Oceanography*. DOI 10.1175/JPO-D-19-0168.1.

Bühler, O., and M. Holmes-Cerfon, 2011: Decay of an internal tide due to random topography in the ocean. *Journal of Fluid Mechanics*, **678**, 271–293, doi:10.1017/jfm.2011.115.

Bühler, O., and M. E. McIntyre, 2005: Wave capture and wave-vortex duality. *Journal of Fluid Mechanics*, **534**, 67–95, doi:10.1017/S0022112005004374.

Byun, S. S., J. J. Park, K. I. Chang, and R. W. Schmitt, 2010: Observation of near-inertial wave reflections within the thermostad layer of an anticyclonic mesoscale eddy. *Geophysical Research Letters*, **37 (1)**, 1–6, doi:10.1029/2009GL041601.

Chelton, D. B., R. A. DeSzoeke, M. G. Schlax, K. El Naggar, and N. Siwertz, 1998: Geographical Variability of the First Baroclinic Rossby Radius of Deformation. *Journal of Physical Oceanography*, **28 (3)**, 433–460, doi:10.1175/1520-0485(1998)028⟨0433:GVOTFB⟩2.0.CO;2.

Chelton, D. B., M. G. Schlax, and R. M. Samelson, 2011: Global observations of nonlinear mesoscale eddies. *Progress in Oceanography*, **91 (2)**, 167–216, doi:10.1016/j.pocean.2011.01.002.

Chelton, D. B., M. G. Schlax, R. M. Samelson, and R. A. de Szoeke, 2007: Global observations of large oceanic eddies. *Geophysical Research Letters*, **34 (15)**, 1–5, doi:10.1029/2007GL030812.

Clément, L., E. Frajka-Williams, K. L. Sheen, J. A. Brearley, and A. C. N. Garabato, 2016: Generation of internal waves by eddies impinging on the western boundary of the North Atlantic. *Journal of Physical Oceanography*, **46 (4)**, 1067–1079, doi:10.1175/JPO-D-14-0241.1.

Danabasoglu, G., and Coauthors, 2014: North Atlantic simulations in Coordinated Ocean-ice Reference Experiments phase II (CORE-II). Part I: Mean states. *Ocean Modelling*, **73**, 76–107, doi:10.1016/j.ocemod.2013.10.005.

Accepted for publication in *Journal of Physical Oceanography*. DOI 10.1175/JPO-D-19-0168.1.

D'Asaro, E. A., 1988: Observations of small eddies in the Beaufort Sea. *Journal of Geophysical Research*, **93 (C6)**, 6669, doi:10.1029/jc093ic06p06669.

D'Asaro, E. A., and R.-C. Lien, 2000: The Wave–Turbulence Transition for Stratified Flows. *Journal of Physical Oceanography*, **30 (7)**, 1669–1678, doi:10.1175/1520-0485(2000)030⟨1669:TWTTFS⟩2.0.CO;2.

de Lavergne, C., S. Falahat, G. Madec, F. Roquet, J. Nycander, and C. Vic, 2019: Toward global maps of internal tide energy sinks. *Ocean Modelling*, **137**, 52–75, doi:10.1016/j.ocemod.2019.03.010.

Dee, D. P., and Coauthors, 2011: The ERA-Interim reanalysis: Configuration and performance of the data assimilation system. *Quarterly Journal of the Royal Meteorological Society*, **137 (656)**, 553–597, doi:10.1002/qj.828.

Dewar, W. K., and H. Meng, 1995: The propagation of submesoscale coherent vortices. *Journal of Physical Oceanography*, **25 (8)**, 1745–1770, doi:10.1175/1520-0485(1995)025⟨1745:TPOSCV⟩2.0.CO;2.

Dugan, J. P., R. P. Mied, P. C. Mignerey, and A. F. Schuetz, 1982: Compact, intrathermocline eddies in the Sargasso Sea. *Journal of Geophysical Research*, **87 (C1)**, 385–393, doi:10.1029/JC087iC01p00385.

Dunphy, M., and K. G. Lamb, 2014: Focusing and vertical mode scattering of the first mode internal tide by mesoscale eddy interaction. *Journal of Geophysical Research: Oceans*, **119 (1)**, 523–536, doi:10.1002/2013JC009293.

Accepted for publication in *Journal of Physical Oceanography*. DOI 10.1175/JPO-D-19-0168.1.

Eden, C., and D. Olbers, 2014: An energy compartment model for propagation, nonlinear interaction, and dissipation of internal gravity waves. *Journal of Physical Oceanography*, **44 (8)**, 2093–2106, doi:10.1175/jpo-d-13-0224.1.

Egbert, G. D., and R. D. Ray, 2000: Significant dissipation of tidal energy in the deep ocean inferred from satellite altimeter data. *Nature*, **405**, 775–778.

Eriksen, C. C., T. J. Osse, R. D. Light, T. Wen, T. W. Lehman, P. L. Sabin, J. W. Ballard, and A. M. Chiodi, 2001: Seaglider: A long-range autonomous underwater vehicle for oceanographic research. *IEEE Journal of Oceanic Engineering*, **26 (4)**, 424–436, doi:10.1109/48.972073.

Evans, D. G., and Coauthors, 2018: Annual cycle of turbulent dissipation estimated from Seagliders. *Geophysical Research Letters*, **45 (10)**, 10 560–10 569, doi:10.1029/2018GL079966.

Fer, I., A. Bosse, B. Ferron, and P. Bouruet-Aubertot, 2018: The dissipation of kinetic energy in the Lofoten Basin eddy. *Journal of Physical Oceanography*, **48 (6)**, 1299–1316, doi:10.1175/jpo-d-17-0244.1.

Ferrari, R., and C. Wunsch, 2009: Ocean circulation kinetic energy: reservoirs, sources, and sinks. *Annual Review of Fluid Mechanics*, **41 (1)**, 253–282, doi:10.1146/annurev.fluid.40.111406.102139.

Forget, G., G. Maze, M. Buckley, and J. Marshall, 2011: Estimated seasonal cycle of North Atlantic Eighteen Degree water volume. *Journal of Physical Oceanography*, **41 (2)**, 269–286, doi:10.1175/2010JPO4257.1.

Forryan, A., J. T. Allen, E. Edhouse, B. Silburn, K. Reeve, and E. Tesi, 2012: Turbulent mixing in the eddy transport of Western Mediterranean Intermediate Water to the Alboran Sea. *Journal of Geophysical Research: Oceans*, **117 (9)**, 1–9, doi:10.1029/2012JC008284.

Accepted for publication in *Journal of Physical Oceanography*. DOI 10.1175/JPO-D-19-0168.1.

Frajka-Williams, E., C. C. Eriksen, P. B. Rhines, and R. R. Harcourt, 2011: Determining vertical water velocities from Seaglider. *Journal of Atmospheric and Oceanic Technology*, **28 (12)**, 1641–1656, doi:10.1175/2011JTECHO830.1.

Fratantoni, D. M., Y. O. Kwon, and B. A. Hodges, 2013: Direct observation of subtropical mode water circulation in the western North Atlantic Ocean. *Deep-Sea Research Part II: Topical Studies in Oceanography*, **91**, 35–56, doi:10.1016/j.dsr2.2013.02.027.

Garcia, H. E., and Coauthors, 2013: World Ocean Atlas 2013. Volume 3: dissolved oxygen, apparent oxygen utilization, and oxygen saturation. *NOAA Atlas NESDIS 75*, **3 (September)**, 27.

Gargett, A. E., 1999: Velcro measurement of turbulence kinetic energy dissipation rate ε. *Journal of Atmospheric and Oceanic Technology*, **16 (12)**, 1973–1993, doi:10.1175/1520-0426(1999)016⟨1973:VMOTKE⟩2.0.CO;2.

Garrett, C., and W. Munk, 1979: Internal waves in the Ocean. *Annual Review of Fluid Mechanics*, **11 (1)**, 339–369, doi:10.1146/annurev.fl.11.010179.002011, URL http://www.annualreviews.org/doi/10.1146/annurev.fl.11.010179.002011.

Gill, A. E., 1982: *Atmosphere-Ocean Dynamics*. Academic Press, New York, 662 pp.

Gregg, M. C., 1989: Scaling turbulent dissipation in the thermocline. *J. Geophys. Res.*, **94 (C7)**, 9686–9698, doi:10.1029/JC094iC07p09686.

Gregg, M. C., and T. B. Sanford, 1988: The dependence of turbulent dissipation on stratification in a diffusively stable thermocline. *Journal of Geophysical Research*, **93 (C10)**, 12 381, doi:10.1029/JC093iC10p12381.

Accepted for publication in *Journal of Physical Oceanography*. DOI 10.1175/JPO-D-19-0168.1.

Hanawa, K., and L. D. Talley, 2001: Mode waters. *Ocean circulation and Climate*, Academic Press, 373–386.

Hebert, D., 1988: The available potential energy of an isolated feature. *Journal of Geophysical Research*, **93 (C1)**, 556, doi:10.1029/JC093iC01p00556.

Henyey, F. S., J. Wright, and S. M. Flatté, 1986: Energy and action flow through the internal wave field: An eikonal approach. *J. Geophys. Res.*, **91 (C7)**, 8487–8495, doi:10.1029/JC091iC07p08487.

Huang, X., Z. Wang, Z. Zhang, Y. Yang, C. Zhou, Q. Yang, W. Zhao, and J. Tian, 2018: Role of mesoscale eddies in modulating the semidiurnal internal tide: Observation results in the northern South China Sea. *Journal of Physical Oceanography*, **48 (8)**, 1749–1770, doi:10.1175/JPO-D-17-0209.1.

Joyce, T. M., J. M. Toole, P. Klein, and L. N. Thomas, 2013: A near-inertial mode observed within a Gulf Stream warm-core ring. *Journal of Geophysical Research: Oceans*, **118 (4)**, 1797–1806, doi:10.1002/jgrc.20141.

Kelly, S. M., N. L. Jones, J. D. Nash, and A. F. Waterhouse, 2013: The geography of semidiurnal mode-1 internal-tide energy loss. *Geophysical Research Letters*, **40 (17)**, 4689–4693, doi:10.1002/grl.50872.

Kerry, C. G., B. S. Powell, and G. S. Carter, 2014: The impact of subtidal circulation on internal-tide-induced mixing in the Philippine Sea. *Journal of Physical Oceanography*, **44 (12)**, 3209–3224, doi:10.1175/jpo-d-13-0249.1.

Accepted for publication in *Journal of Physical Oceanography*. DOI 10.1175/JPO-D-19-0168.1.

Kolmogorov, A. N., 1941: The local structure of turbulence in incompressible viscous fluid for very large Reynolds numbers. *Proceedings of the Royal Society A: Mathematical, Physical and Engineering Sciences*, **434 (1890)**, 9–13, doi:10.1098/rspa.1991.0075.

Kunze, E., 1985: Near-inertial wave propagation In geostrophic shear. *Journal of Physical Oceanography*, **15 (5)**, 544–565, doi:10.1175/1520-0485(1985)015⟨0544:NIWPIG⟩2.0.CO;2, URL http://journals.ametsoc.org/doi/abs/10.1175/1520-0485%281985%29015%3C0544%3ANIWPIG%3E2.0.CO%3B2.

Kunze, E., 2017: Internal-wave-driven mixing: Global geography and budgets. *Journal of Physical Oceanography*, **47 (6)**, 1325–1345, doi:10.1175/JPO-D-16-0141.1.

Kunze, E., R. W. Schmitt, and J. M. Toole, 1995: The energy balance in a warm-core ring's near-inertial critical layer. *Journal of Physical Oceanography*, **25 (5)**, 942–957, doi:10.1175/1520-0485(1995)025⟨0942:tebiaw⟩2.0.co;2.

Ledwell, J. R., D. J. McGillicuddy, and L. a. Anderson, 2008: Nutrient flux into an intense deep chlorophyll layer in a mode-water eddy. *Deep-Sea Research Part II: Topical Studies in Oceanography*, **55 (10-13)**, 1139–1160, doi:10.1016/j.dsr2.2008.02.005.

Legg, S., and A. Adcroft, 2003: Internal wave breaking at concave and convex continental slopes. *Journal of Physical Oceanography*, **33 (11)**, 2224–2246, doi:10.1175/1520-0485(2003)033⟨2224:iwbaca⟩2.0.co;2.

Li, C., Z. Zhang, W. Zhao, and J. Tian, 2017: A statistical study on the subthermocline submesoscale eddies in the northwestern Pacific Ocean based on Argo data. *Journal of Geophysical Research: Oceans*, **122**, 3586–3598, doi:10.1002/2016JC012561.

Lighthill, M. J., 1978: *Waves in fluids*. Cambridge University Press, 504 pp.

Accepted for publication in *Journal of Physical Oceanography*. DOI 10.1175/JPO-D-19-0168.1.

Locarnini, R. A., and Coauthors, 2013: World Ocean Atlas 2013. Vol. 1: Temperature. *S. Levitus, Ed.; A. Mishonov, Technical Ed.; NOAA Atlas NESDIS*, **73 (September)**, 40, doi: 10.1182/blood-2011-06-357442.

Lonergan, L., and N. White, 1997: Origin of the Betic-Rif mountain belt. *Tectonics*, **16 (3)**, 504–522, doi:10.1029/96TC03937.

Lueck, R., and T. Osborn, 1986: The dissipation of kinetic energy in a warm-core ring. *Journal of Geophysical Research*, **91 (C1)**, 803–818, doi:10.1029/jc091ic01p00803.

MacKinnon, J. A., and M. C. Gregg, 2003: Shear and baroclinic energy flux on the summer new England shelf. *Journal of Physical Oceanography*, **33 (7)**, 1462–1475, doi:10.1175/1520-0485(2003)033⟨1462:SABEFO⟩2.0.CO;2.

MacKinnon, J. A., and Coauthors, 2017: Climate Process Team on internal-wave driven ocean mixing. *Bulletin of the American Meteorological Society*, 2429–2454, doi:10.1175/BAMS-D-16-0030.1.

Martínez-Marrero, A., and Coauthors, 2019: Near-inertial wave trapping near the base of an anticyclonic mesoscale eddy under normal atmospheric conditions. *Journal of Geophysical Research: Oceans*, **124 (11)**, 8455–8467, doi:10.1029/2019JC015168.

McGillicuddy, D. J., 2015: Formation of intrathermocline lenses by eddy-wind interaction. *Journal of Physical Oceanography*, **45 (2)**, 606–612, doi:10.1175/JPO-D-14-0221.1.

McGillicuddy, D. J., and Coauthors, 2007: Eddy/Wind interactions stimulate extraordinary mid-ocean plankton blooms. *Science*, **316 (5827)**, 1021–1026, doi:10.1126/science.1136256.

McWilliams, J. C., 1985: Submesoscale, coherent vortices in the ocean. *Reviews of Geophysics*, **23 (2)**, 165–182, doi:10.1029/RG023i002p00165.

Accepted for publication in *Journal of Physical Oceanography*. DOI 10.1175/JPO-D-19-0168.1.

Melet, A., R. Hallberg, S. Legg, and M. Nikurashin, 2013: Sensitivity of the ocean state to lee wave–driven mixing. *Journal of Physical Oceanography*, **44 (3)**, 900–921, doi:10.1175/jpo-d-13-072.1.

Melet, A., S. Legg, and R. Hallberg, 2016: Climatic impacts of parameterized local and remote tidal mixing. *Journal of Climate*, **29 (10)**, 3473–3500, doi:10.1175/JCLI-D-15-0153.1.

Meunier, T., E. Pallás-Sanz, M. Tenreiro, E. Portela, J. Ochoa, A. Ruiz-Angulo, and S. Cusí, 2018a: The vertical structure of a Loop Current eddy. *Journal of Geophysical Research: Oceans*, **123 (9)**, 6070–6090, doi:10.1029/2018JC013801.

Meunier, T., and Coauthors, 2018b: Intrathermocline eddies embedded within an anticyclonic vortex ring. *Geophysical Research Letters*, **45 (15)**, 7624–7633, doi:10.1029/2018GL077527.

Mooers, C. N., 1975: Several effects of baroclinic currents on the three-dimensional propagation of inertial-internal waves†. *Geophysical Fluid Dynamics*, **6 (3)**, 277–284, doi:10.1080/03091927509365798.

Moum, J. N., 1996: Energy-containing scales of turbulence in the ocean thermocline. *Journal of Geophysical Research: Oceans*, **101 (C6)**, 14 095–14 109, doi:10.1029/96jc00507.

Müller, P., G. Holloway, F. Henyey, and N. Pomphrey, 1986: Nonlinear interactions among internal gravity waves. *Reviews of Geophysics*, **24 (3)**, 493–536, doi:10.1029/RG024i003p00493.

Müller, P., and N. Xu, 1992: Scattering of oceanic internal gravity waves off random bottom topography. *Journal of Physical Oceanography*, **22 (5)**, 474–488, doi:10.1175/1520-0485(1992)022⟨0474:sooigw⟩2.0.co;2.

Accepted for publication in *Journal of Physical Oceanography*. DOI 10.1175/JPO-D-19-0168.1.

Munk, W., 1981: Internal waves and small-Scale process, in Evolution of physical oceanography: Scientific surveys in honor of Henry Stommel. *MIT Press, Cambridge, Mass*, 264–291, doi:10.1121/1.3425741.

Munk, W., and C. Wunsch, 1998: Abyssal recipes II : energetics of tidal and wind mixing. *Deep Sea Research I*, **45 (1998)**, 1977–2010.

Nash, J. D., S. M. Kelly, E. L. Shroyer, J. N. Moum, and T. F. Duda, 2012: The unpredictable nature of internal tides on continental shelves. *Journal of Physical Oceanography*, **42 (11)**, 1981–2000, doi:10.1175/JPO-D-12-028.1.

Nash, J. D., E. Kunze, J. M. Toole, and R. W. Schmitt, 2004: Internal tide reflection and turbulent mixing on the continental slope. *Journal of Physical Oceanography*, **34 (5)**, 1117–1134, doi:10.1175/1520-0485(2004)034⟨1117:ITRATM⟩2.0.CO;2, URL http://journals.ametsoc.org/doi/abs/10.1175/1520-0485%282004%29034%3C1117%3AITRATM%3E2.0.CO%3B2.

Nycander, J., 2005: Generation of internal waves in the deep ocean by tides. *Journal of Geophysical Research C: Oceans*, **110 (10)**, 1–9, doi:10.1029/2004JC002487.

Oakey, N. S., 1982: Determination of the rate of dissipation of turbulent energy from simultaneous temperature and velocity shear microstructure measurements. *J. Phys. Oceanogr*, **12 (3)**, 256–271, doi:10.1175/1520-0485(1982)012⟨0256:DOTROD⟩2.0.CO;2.

Olbers, D. J., 1976: Nonlinear energy transfer and the energy balance of the internal wave field in the deep ocean. *Journal of Fluid Mechanics*, **74 (2)**, 375–399, doi:10.1017/s0022112076001857.

Accepted for publication in *Journal of Physical Oceanography*. DOI 10.1175/JPO-D-19-0168.1.

Olbers, D. J., 1981: The propagation of internal waves in a geostrophic current. *Journal of Physical Oceanography*, **11 (9)**, 1224–1233, doi:10.1175/1520-0485(1981)011⟨1224:TPOIWI⟩2.0.CO;2.

Olson, D. B., R. W. Schmitt, M. Kennelly, and T. M. Joyce, 1985: A two-layer diagnostic model of the long-term physical evolution of warm-core ring 82B. *Journal of Geophysical Research*, **90 (C5)**, 8813, doi:10.1029/jc090ic05p08813.

Peters, H., M. C. Gregg, and T. B. Sanford, 1995: Detail and scaling of turbulent Equatorial Undercurrent. *Journal of Geophysical Research*, **100 (C9)**, 18 349–18 368.

Polzin, K. L., 2010: Mesoscale Eddy–Internal Wave Coupling. Part II: Energetics and Results from PolyMode. *Journal of Physical Oceanography*, **40 (4)**, 789–801, doi:10.1175/2009jpo4039.1.

Prater, M. D., and T. B. Sanford, 1994: A Meddy off Cape St. Vincent. Part I: Description. *Journal of Physical Oceanography*, **24 (7)**, 1572–1586, doi:10.1175/1520-0485(1994)024⟨1572:AMOCSV⟩2.0.CO;2.

Rainville, L., and R. Pinkel, 2006: Propagation of low-mode internal waves through the Ocean. *Journal of Physical Oceanography*, **36 (6)**, 1220–1236, doi:10.1175/jpo2889.1.

Reverdin, G., J. C. Gascard, B. Le Cann, L. Prieur, M. Assenbaum, and P. Lherminier, 2009: A long-lasting mode water vortex in the Northeast Atlantic Ocean. *Journal of Physical Oceanography*, **39 (3)**, 536–558, doi:10.1175/2008JPO3970.1.

Schütte, F., P. Brandt, and J. Karstensen, 2016: Occurrence and characteristics of mesoscale eddies in the tropical northeastern Atlantic Ocean. *Ocean Science*, **12 (3)**, 663–685, doi:10.5194/os-12-663-2016.

Accepted for publication in *Journal of Physical Oceanography*. DOI 10.1175/JPO-D-19-0168.1.

Sheen, K. L., J. A. Brearley, A. C. Naveira Garabato, D. A. Smeed, L. St. Laurent, M. P. Meredith, A. M. Thurnherr, and S. Waterman, 2015: Modification of turbulent dissipation rates by a deep Southern Ocean eddy. *Geophysical Research Letters*, **42 (May)**, 3450–3457, doi: 10.1002/2015GL063216.

Smith, K. S., 2007: The geography of linear baroclinic instability in Earth's oceans. *Journal of Marine Research*, **65 (5)**, 655–683, doi:10.1357/002224007783649484.

Speer, K., and G. Forget, 2013: *Global distribution and formation of mode waters*, Vol. 103. 2nd ed., MIT Press, 211–226 pp., doi:10.1016/B978-0-12-391851-2.00009-X.

St. Laurent, L. C., and C. Garrett, 2002: The role of internal tides in mixing the deep ocean. *Journal of Physical Oceanography*, **32 (10)**, 2882–2899, doi:10.1175/1520-0485(2002)032⟨2882:TROITI⟩2.0.CO;2.

Todd, R. E., D. L. Rudnick, J. T. Sherman, W. Brechner Owens, and L. George, 2017: Absolute velocity estimates from autonomous underwater gliders equipped with doppler current profilers. *Journal of Atmospheric and Oceanic Technology*, **34 (2)**, 309–333, doi:10.1175/JTECH-D-16-0156.1.

Vic, C., and Coauthors, 2019: Deep-ocean mixing driven by small-scale internal tides. *Nature Communications*, **10 (1)**, 2099, doi:10.1038/s41467-019-10149-5.

Waterhouse, A. F., and Coauthors, 2014: Global patterns of diapycnal mixing from measurements of the turbulent dissipation rate. *Journal of Physical Oceanography*, **44 (7)**, 1854–1872, doi: 10.1175/JPO-D-13-0104.1.

Weller, R. A., 1982: The relation of near-inertial motions observed in the mixed layer during the JASIN (1978) Experiment to the local wind stress and to the quasi-geostrophic flow field.

Accepted for publication in *Journal of Physical Oceanography*. DOI 10.1175/JPO-D-19-0168.1.

Journal of Physical Oceanography, **12**, 1122–1136, doi:10.1175/1520-0485(1982)012⟨1122:TRONIM⟩2.0.CO;2.

Whalen, C. B., J. A. MacKinnon, and L. D. Talley, 2018: Large-scale impacts of the mesoscale environment on mixing from wind-driven internal waves. *Nature Geoscience*, **11 (11)**, 842–847, doi:10.1038/s41561-018-0213-6.

Whalen, C. B., L. D. Talley, and J. A. MacKinnon, 2012: Spatial and temporal variability of global ocean mixing inferred from Argo profiles. *Geophysical Research Letters*, **39 (17)**, 1–6, doi:10.1029/2012GL053196.

Whitt, D. B., and L. N. Thomas, 2013: Near-inertial waves in strongly baroclinic currents. *Journal of Physical Oceanography*, **43 (4)**, 706–725, doi:10.1175/JPO-D-12-0132.1.

Wunsch, C., and R. Ferrari, 2004: Vertical mixing, energy, and the general circulation of the oceans. *Annual Review of Fluid Mechanics*, **36 (1)**, 281–314, doi:10.1146/annurev.fluid.36.050802.122121.

Xu, L., P. Li, S. P. Xie, Q. Liu, C. Liu, and W. Gao, 2016: Observing mesoscale eddy effects on mode-water subduction and transport in the North Pacific. *Nature Communications*, **7**, 1–9, doi:10.1038/ncomms10505.

Zhang, Z., P. Li, L. Xu, C. Li, W. Zhao, J. Tian, and T. Qu, 2015: Subthermocline eddies observed by rapid-sampling Argo floats in the subtropical northwestern Pacific Ocean in Spring 2014. *Geophysical Research Letters*, **42**, 6438–6445, doi:10.1002/2015GL064601.

Zhang, Z., Z. Liu, K. Richards, G. Shang, W. Zhao, J. Tian, X. Huang, and C. Zhou, 2019: Elevated diapycnal mixing by a subthermocline eddy in the western Equatorial Pacific. *Geophysical Research Letters*, **46 (5)**, 2628–2636, doi:10.1029/2018GL081512.

Accepted for publication in *Journal of Physical Oceanography*. DOI 10.1175/JPO-D-19-0168.1.

Zhang, Z., B. Qiu, J. Tian, W. Zhao, and X. Huang, 2018: Latitude-dependent finescale turbulent shear generations in the Pacific tropical-extratropical upper ocean. *Nature Communications*, **9 (1)**, doi:10.1038/s41467-018-06260-8.

Zhang, Z., Y. Zhang, and W. Wang, 2017: Three-compartment structure of subsurface-intensified mesoscale eddies in the ocean. *Journal of Geophysical Research: Oceans*, **122**, 1653–1664, doi:10.1002/2016JC012376.

Zhao, Z., M. H. Alford, J. B. Girton, L. Rainville, and H. L. Simmons, 2016: Global observations of open-ocean mode-1 M2 internal tides. *Journal of Physical Oceanography*, **46 (6)**, 1657–1684, doi:10.1175/JPO-D-15-0105.1.

Zhao, Z., M. H. Alford, J. A. MacKinnon, and R. Pinkel, 2009: Long-range propagation of the semidiurnal internal tide from the Hawaiian Ridge. *Journal of Physical Oceanography*, **40 (4)**, 713–736, doi:10.1175/2009jpo4207.1.

Zweng, M. M., and Coauthors, 2013: World Ocean Atlas 2013, Volume 2: Salinity. *NOAA Atlas NESDIS*, **2 (1)**, 39, doi:10.1182/blood-2011-06-357442.

Accepted for publication in *Journal of Physical Oceanography*. DOI 10.1175/JPO-D-19-0168.1.

LIST OF FIGURES

Accepted for publication in *Journal of Physical Oceanography*. DOI 10.1175/JPO-D-19-0168.1.

Accepted for publication in *Journal of Physical Oceanography*. DOI 10.1175/JPO-D-19-0168.1.

Accepted for publication in *Journal of Physical Oceanography*. DOI 10.1175/JPO-D-19-0168.1.

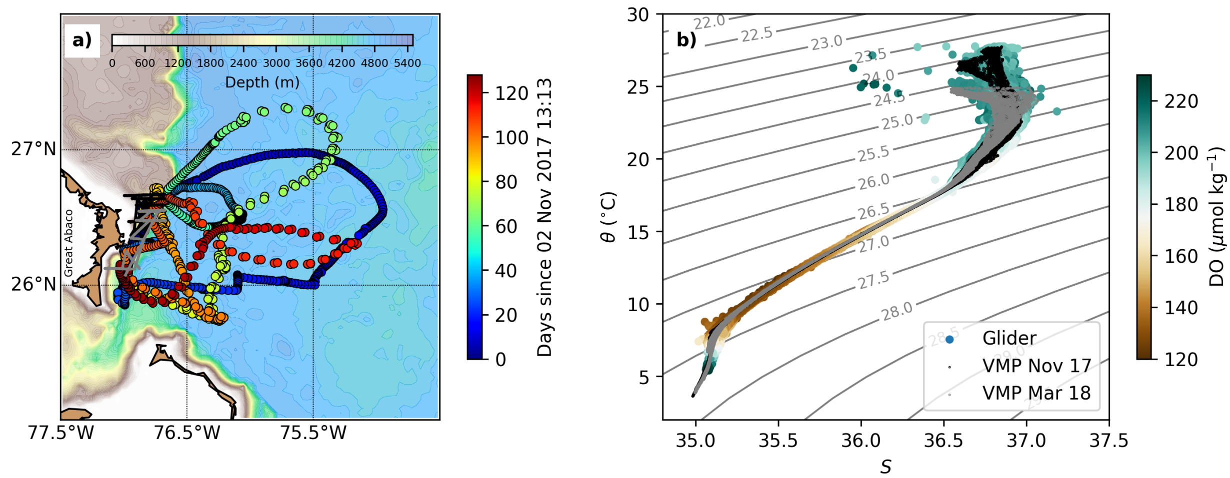

FIG. 1. (a) Trajectory of the sg534 Seaglider between 7 November 2017 and 10 March 2018 (circles) and stations sampled with the CTD mounted on the Vertical Microstructure Profilers (VMP) during the deployment and recovery cruises, MerMEED II (WS17305, November 2017, black dots) and MerMEED III (WS18066, March 2019, gray dots), respectively. Bathymetry from the 2-Minute Gridded Global Relief Data ETOPO2v2 (`doi:10.7289/V5J1012Q`) is represented. (b) Potential temperature - salinity diagrams obtained with the sg534 glider (circles) and with the VMP for the deployment and recovery cruises. The dot color code in (b) represents the dissolved oxygen (DO) concentration.

Accepted for publication in *Journal of Physical Oceanography*. DOI 10.1175/JPO-D-19-0168.1.

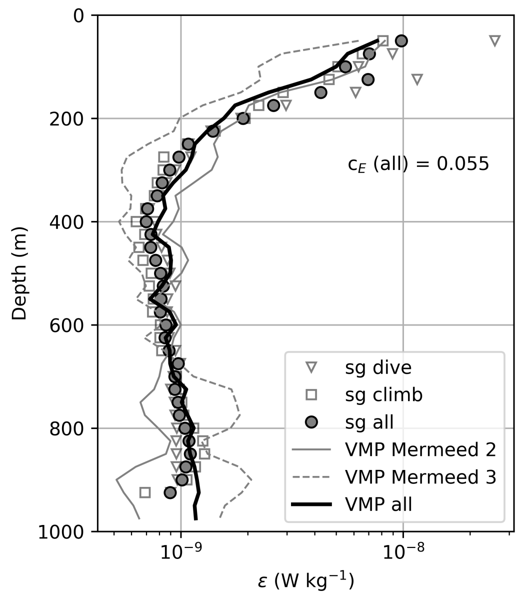

FIG. 2. Comparison of log-averaged ε profiles obtained with the VMP microstructure profiler during the MerMEED cruises (lines: gray-solid for MerMEED II (November), gray-dashed for MerMEED III (March), black for both cruises) and the glider estimates (markers: triangles for dives, squares for climbs and solid circles for both). The value of the c_E constant shown was obtained by least-squares minimization of the difference between the log-averaged profiles.

Accepted for publication in *Journal of Physical Oceanography*. DOI 10.1175/JPO-D-19-0168.1.

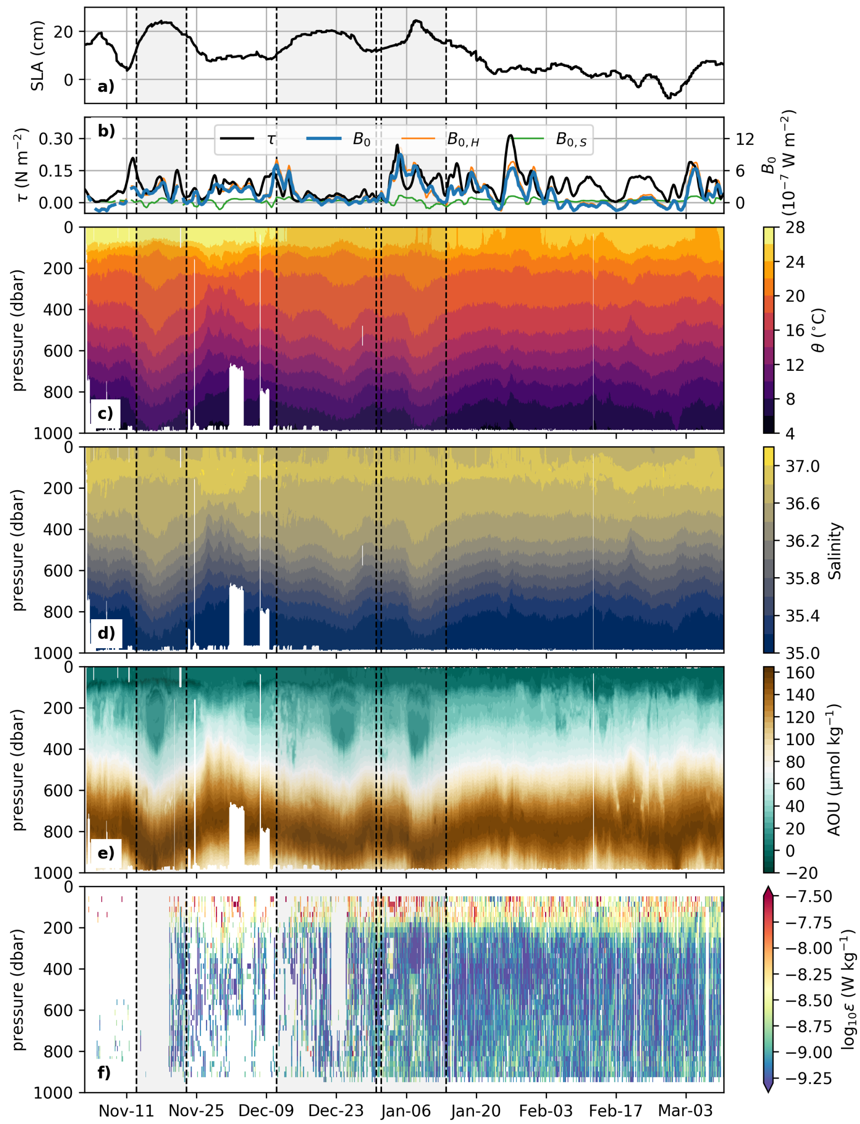

FIG. 3. Time-series of the atmospheric and oceanographic variables during the sg534 glider survey between 26–27°N and 75–77°W, from 7th December 2017 to 10th March 2018. (a) Daily values of satellite-derived sea level anomaly (SLA) interpolated onto the glider position for each sampled profile; (b) daily wind-stress (τ, black) and air-sea buoyancy fluxes of heat ($B_{0,H}$, orange), salt ($B_{0,S}$, green) and total (B_0, blue) from ERA-Interim reanalysis at 26.25°N–75.75°W; and (c,d,e,f) potential temperature (θ), salinity, apparent oxygen utilization (AOU) and TKE dissipation rate (ε) recorded with the Seaglider. 3-hourly atmospheric data in (b) have been smoothed with an 8-point (24 hour) running average to retrieve daily values. Shaded areas enclosed by dashed lines indicate the glider transects that crossed the area of influence of the anticyclonic mesoscale eddy (see glider trajectories in Figure 4)

Accepted for publication in *Journal of Physical Oceanography*. DOI 10.1175/JPO-D-19-0168.1.

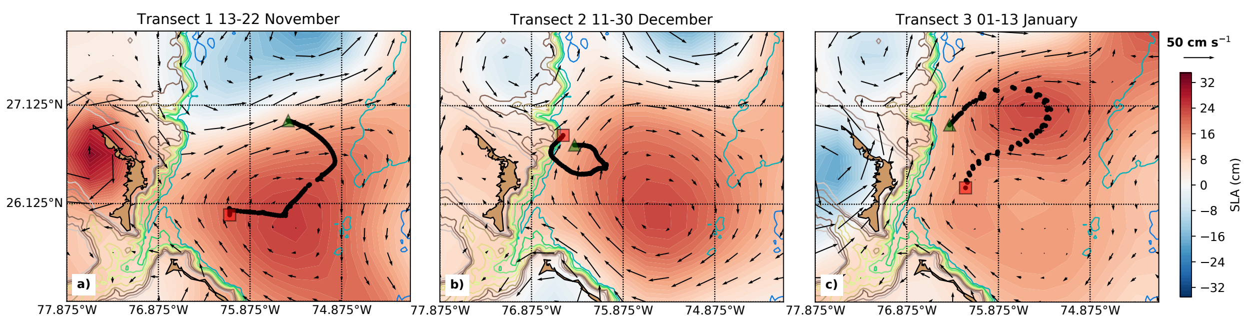

1112 FIG. 4. Maps of averaged sea level anomaly (background color) and surface geostrophic velocity (arrows) during the glider transects that sampled the anticyclonic eddy: a) transect 1 (13–22 November 2017), b) transect 2 (11–30 December 2017) and c) transect 3 (1–13 January 2018). The mean position of the glider during each profile (dives and climbs) are shown as black dots, the first (last) profile of the transect is indicated with a green (red) triangle (square). Bathymetric contours spaced by 500 m are shown between 500 and 5000 m (The color scale is the same as in Figure 1a).

Accepted for publication in *Journal of Physical Oceanography*. DOI 10.1175/JPO-D-19-0168.1.

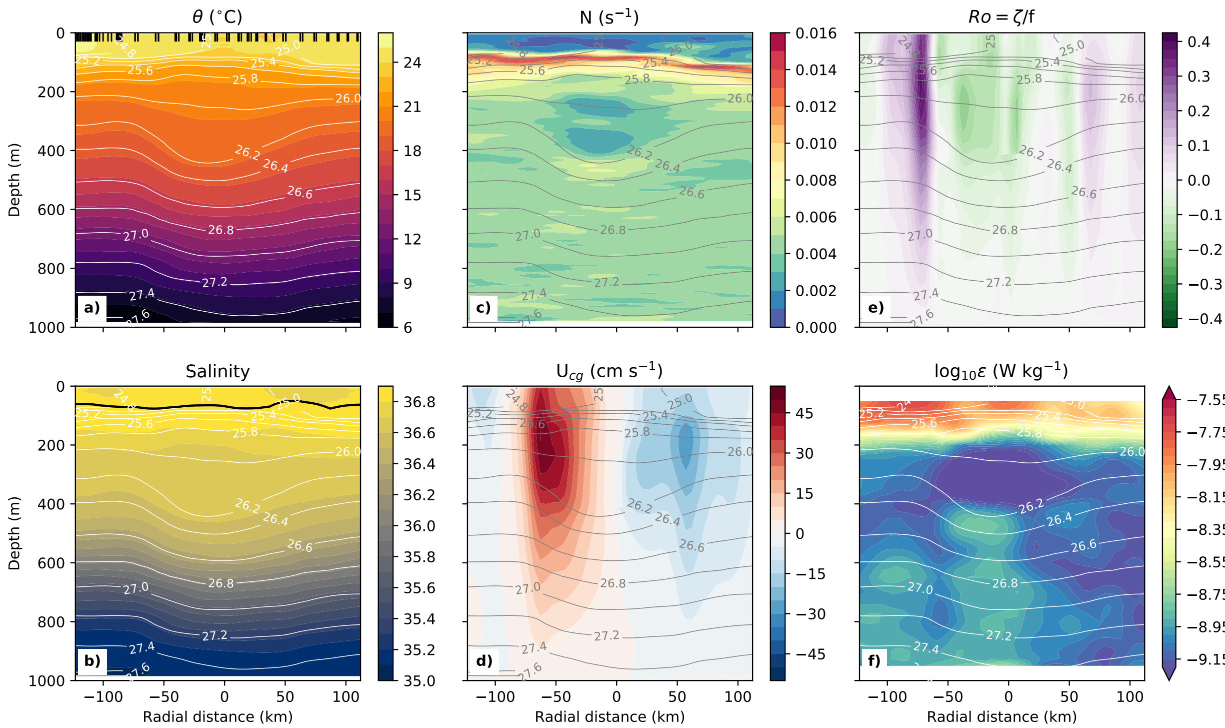

FIG. 5. Radial distribution (with respect to the estimated eddy center) of the grid-averaged properties of the anticyclonic eddy obtained during the third glider transect (1–13 January 2018). (a) Potential temperature (θ), (b) salinity, (c) buoyancy frequency (N), (d) cross-section cyclogeostrophic velocities (U_{cg}), (e) Rossby number ($Ro = \zeta/f$, i.e. vertical vorticity relative to planetary vorticity) and (f) TKE dissipation rate (ε). Potential density anomaly (σ_θ) contours are shown in all the plots. Mixed-layer depth is shown in panel b) as a thick black line. Negative radial distances were assigned to positions sampled in the northwestern flank of the eddy during the first part of the transect. The positions of the original glider profiles are shown as black markers on the top of panel (a).

Accepted for publication in *Journal of Physical Oceanography*. DOI 10.1175/JPO-D-19-0168.1.

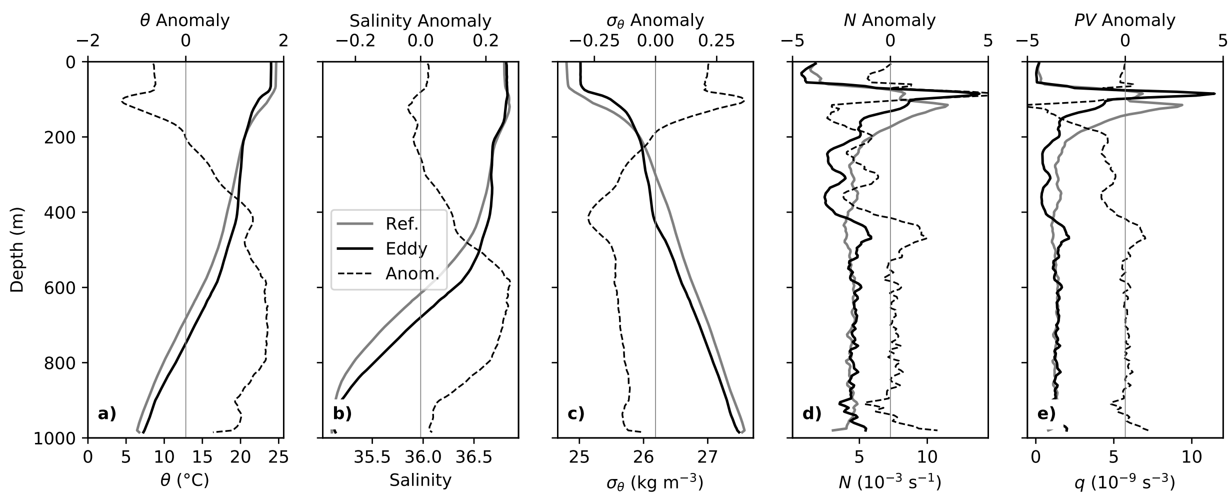

FIG. 6. Mean (a) potential temperature (θ), (b) salinity, (c) potential density anomaly (σ_θ), (d) buoyancy frequency (N) and (e) vertical Ertel potential vorticity (q) in the inner part of the anticyclonic eddy core (black solid line, $r < 15$ km), in the background area unaffected by the eddy (gray solid, $r > 80$ km) and the anomalies within the eddy (black dashed), during the third glider transect across the eddy.

Accepted for publication in *Journal of Physical Oceanography*. DOI 10.1175/JPO-D-19-0168.1.

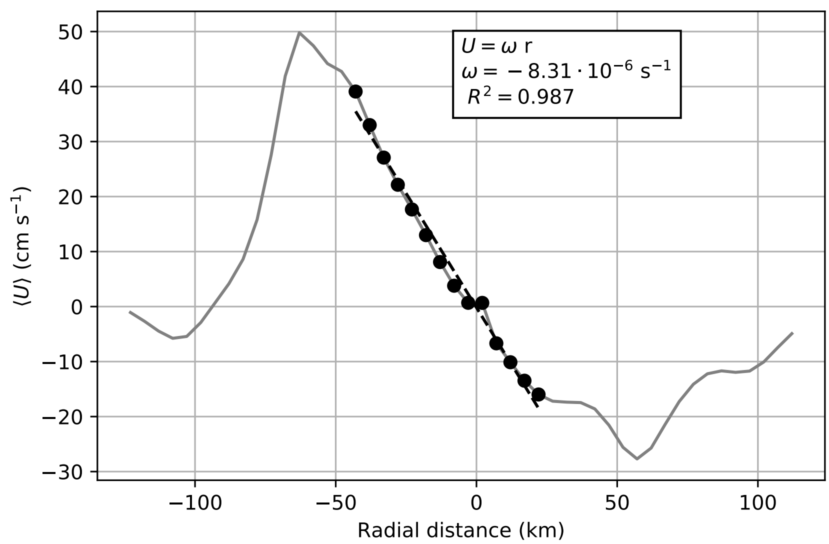

1130 FIG. 7. Radial distribution of mean cyclogeostrophic azimuthal velocities around the velocity maximum (from 130 to 230 m depth) during the third glider transect sampling the anticyclonic eddy. The dashed line represents the linear fit to solid body rotation within the eddy core: $U = \omega r$, where ω is the angular velocity and r is the radial distance.

Accepted for publication in *Journal of Physical Oceanography*. DOI 10.1175/JPO-D-19-0168.1.

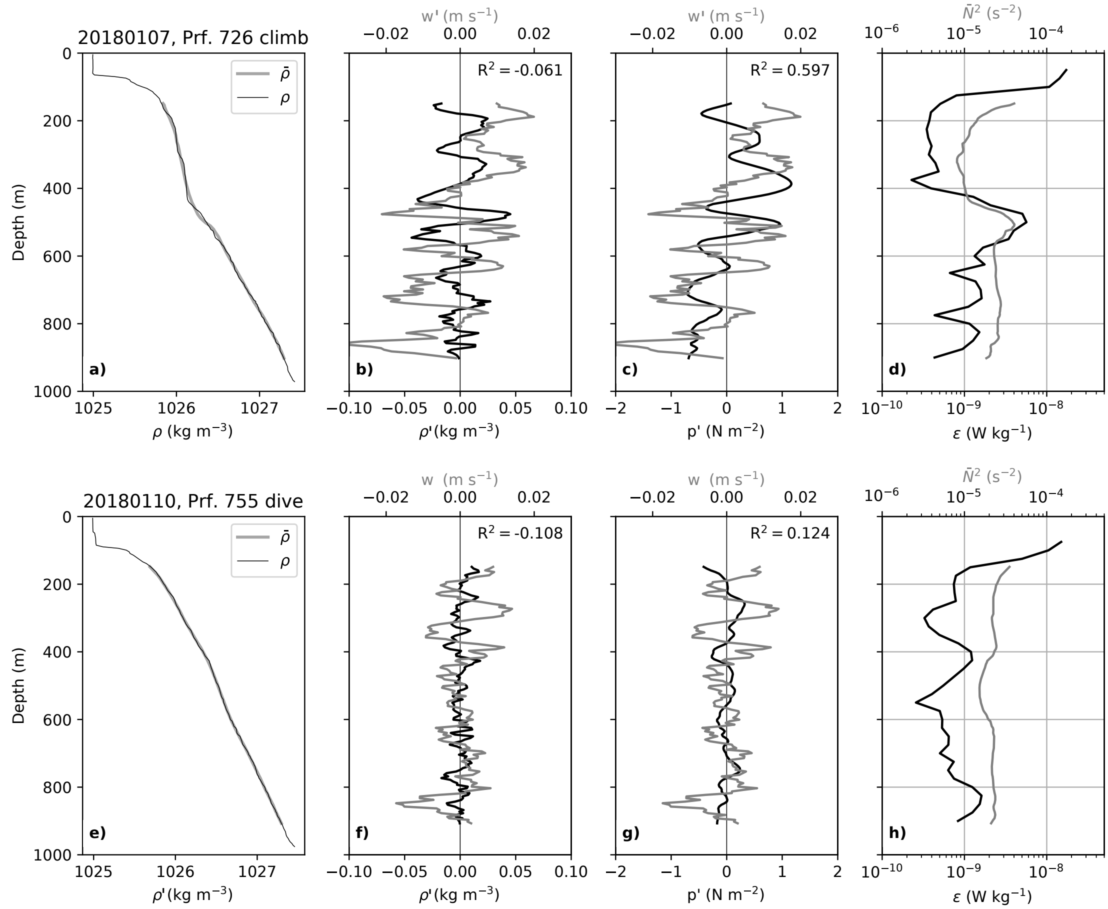

FIG. 8. Examples of wave-like structures observed in two profiles sampled during the third glider transect across the eddy: (a–d) one profile on 7 January, 10 km to the northwest of the eddy center and (e–h) one profile on 10 January, 50 km to the southwest of the eddy center. The black thin line in (a,e) represents the observed potential density profile (ρ), and the gray thick line, the smoothed density profile ($\overline{\rho}$) computed with the Bray and Fofonoff (1981) algorithm. Black lines in (b) and (f) represent the density (ρ') and in (c) and (g) the hydrostatic pressure perturbations (p') calculated using the Bray and Fofonoff (1981) algorithm; gray lines in (b, c, f, g) represent the vertical water velocity (w). In (d) and (h), smoothed buoyancy frequency ($\overline{N}^2$) as computed from the Bray and Fofonoff (1981) algorithm (gray) and TKE dissipation (ε, black) are shown.

Accepted for publication in *Journal of Physical Oceanography*. DOI 10.1175/JPO-D-19-0168.1.

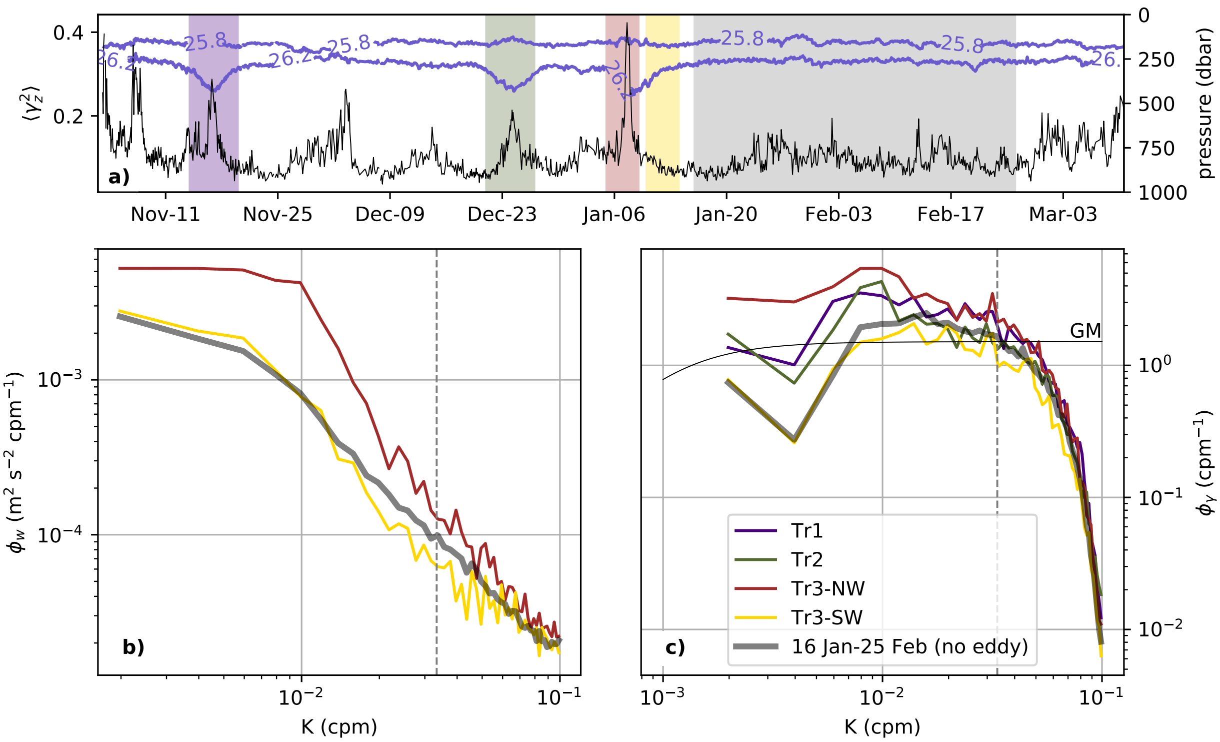

1142 FIG. 9. Vertical strain (γ_z) and vertical water velocity (w) during the Seaglider survey: (a) strain variance between 200 and 1000 m (black) and vertical position of the two isopynals delimiting the anticyclonic eddy core (25.8 kg m^{-3} and 26.2 kg m^{-3}); (b, c) vertical wavenumber power spectra (ϕ) between 200 and 1000 m of w and γ_z, respectively, for the periods indicated by color shading in panel (a). The vertical gray dashed line in panels (b, c) represents the vertical wavelength of 30 m used for high-pass filtering the velocity signal for ε calculations, and GM indicates the Garrett-Munk (Garrett and Munk 1979) strain spectrum in panel (c).

Accepted for publication in *Journal of Physical Oceanography*. DOI 10.1175/JPO-D-19-0168.1.

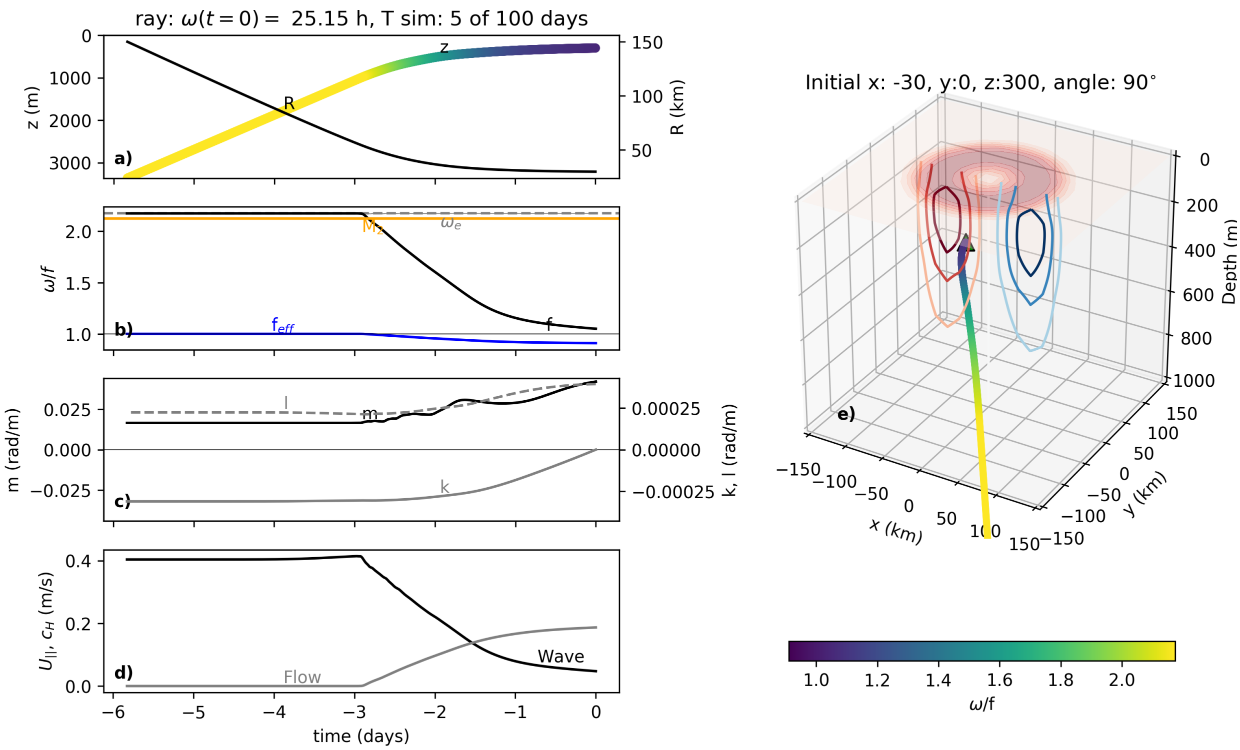

FIG. 10. Internal wave tracing experiment backwards in time using the Kunze (1985) dispersion relation. A wave with $\lambda_z = 150$ m and $\omega = 1.1f$ wave was initially ($t = 0$) released at $z = -300$ m and $x, y = (-30, 0)$ km (eddy center at $x, y = (0, 0)$), with forward energy propagation directed to the north (heading angle 90°) and upward. Time evolution of: (a) vertical position (z, dots with intrinsic frequency ω in color scale) and distance to eddy center (R, black line); (b) inner frequency (ω, black), (c) vertical (m, black) and horizontal (k, l, gray) wavenumbers, and (d) the horizontal have propagation speed (c_H, black line) and the background flow speed projected in the direction of the horizontal propagation of the wave ($U_{||}$, gray line). The three dimensional ray trajectory is outlined in panel (e), with the initial position indicated by a green triangle. In panel (b), the semidiurnal tidal (M_2, orange) and the Eulerian (fixed-frame) ray frequency (ω_e, gray dashed) are also shown. In panel (e), red shading represents the background current speed at the surface and the color contours, the magnitude and direction (positive red) of the velocity across the plane $y = 0$.

Accepted for publication in *Journal of Physical Oceanography*. DOI 10.1175/JPO-D-19-0168.1.

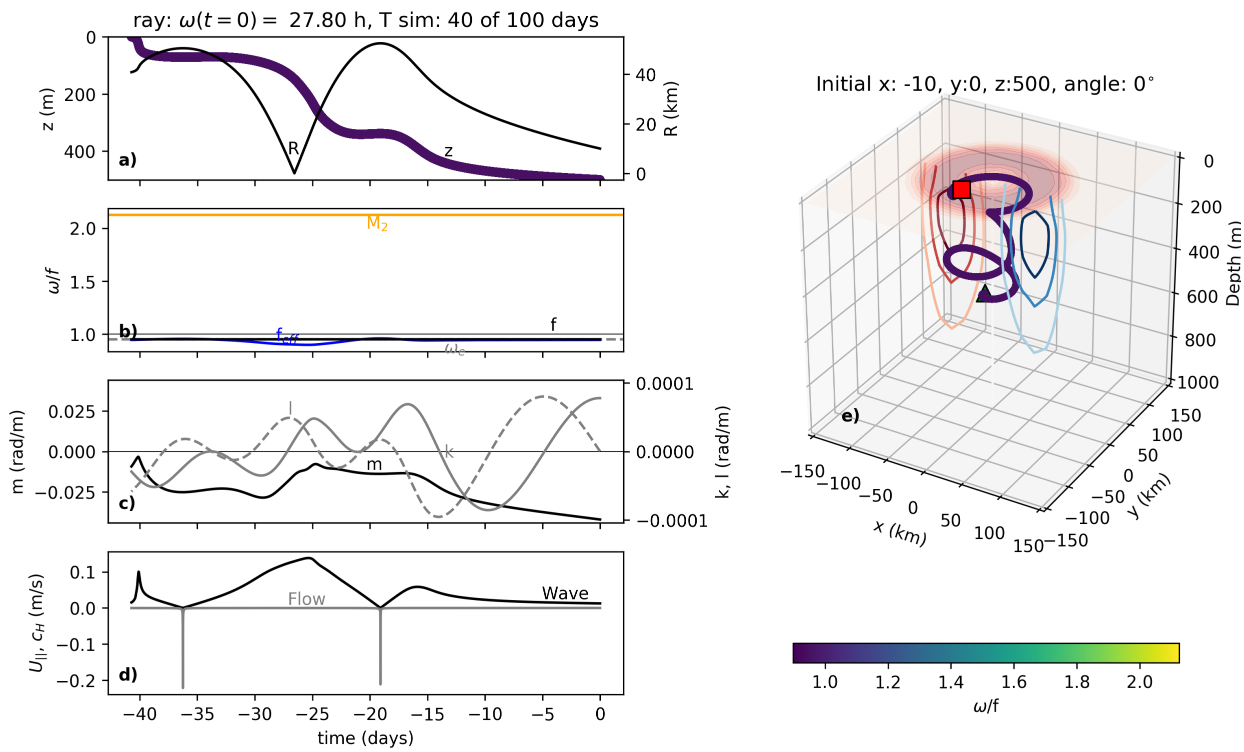

FIG. 11. Internal wave tracing experiment backwards in time using the Kunze (1985) dispersion relation. A wave with $\lambda_z = 150$ m and $\omega = 0.95f$ wave was initially ($t = 0$) released at $z = -500$ m and $x, y = (-10, 0)$ km (eddy center at $x, y = (0, 0)$), with forward energy propagation directed to the east (heading angle 0°) and downward. Time evolution of: (a) vertical position (z, dots with inner frequency ω in color scale) and distance to eddy center (R, black line); (b) inner frequency (ω, black), effective inertial frequency (f_{eff}, blue), (c) vertical (m, black) and horizontal (k, l, gray) wavenumbers, and (d) the horizontal have propagation speed (c_H, black line) and the background flow speed projected in the direction of horizontal propagation of the wave ($U_{||}$, gray line). The three dimensional ray trajectory is outlined in panel (d), with the initial (final) position indicated by a green triangle (red square). In panel (b), the semidiurnal tidal (M_2, orange) and the Eulerian (fixed-frame) ray frequency (ω_e, gray) are also shown. In panel (e), red shading represents the background current speed at the surface and the color contours, the magnitude and direction (positive red) of the velocity across the plane $y = 0$.

Accepted for publication in *Journal of Physical Oceanography*. DOI 10.1175/JPO-D-19-0168.1.

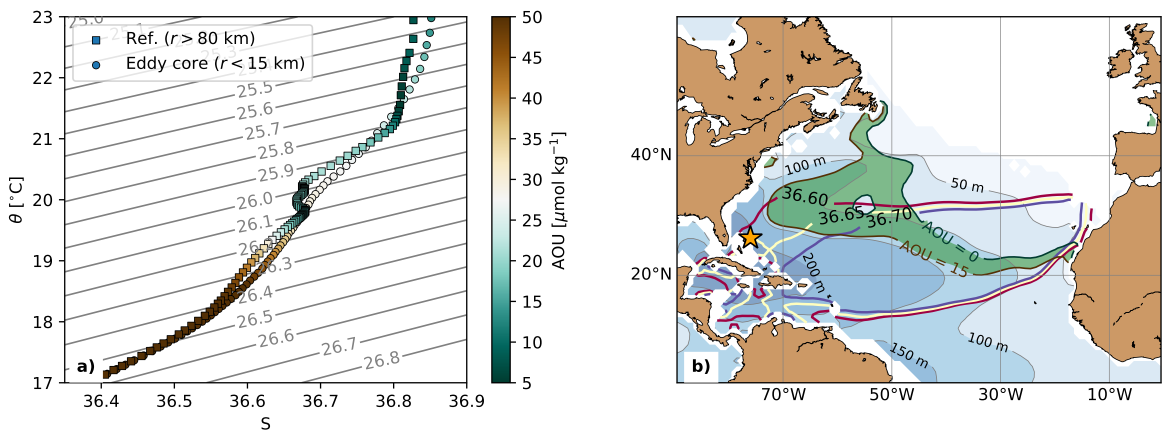

1170 FIG. 12. (a) Potential temperature - salinity diagram during the third transect across the eddy (1–13 January
1171 2018) in the the inner part of the anticyclonic eddy core (circles, $r < 15$ km) and in the background area un-
1172 affected by the eddy (squares, $r > 80$ km); (b) distribution of salinity (red-yellow-blue) contours, AOU (green
1173 shadding) at $\sigma_\theta = 26.05$ kg m^{-3} and depth of this isopycnal in the North Atlantic. Climatological data was ob-
1174 tained form the World Ocean Atlas 2013 (`https://www.nodc.noaa.gov/OC5/WOD13/`). The area covered
1175 by the glider survey is indicated with a yellow star.

Accepted for publication in *Journal of Physical Oceanography*. DOI 10.1175/JPO-D-19-0168.1.

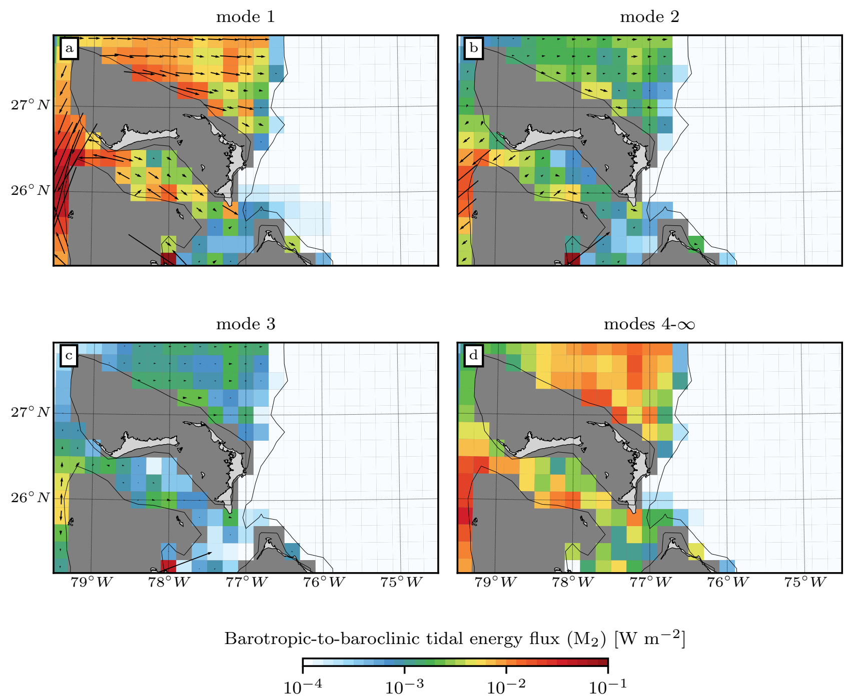

1176 FIG. 13. Barotropic-to-baroclinic energy conversion (internal tide generation fluxes, in colors) for different
1177 internal tide vertical modes in the study region derived from a semi-analytical model for internal tide generation
1178 over topography (Vic et al. 2019). The propagation direction and magnitude of the energy fluxes at the source
1179 are displayed as arrows. Bathymetry shallower than 500 m is shaded gray. This corresponds to areas where the
1180 assumptions underlying the linear conversion model are potentially violated.

Accepted for publication in *Journal of Physical Oceanography*. DOI 10.1175/JPO-D-19-0168.1.